

Dear Dr. Fousseis,

Our paper makes a very important conceptual contribution, in that it highlights how critically low porosity, combined with evidence that solution-precipitation occurred, means a fault is in a critical state. This may be the control on earthquake recurrence interval of many similar faults. We think that your focus (mirrored and thus doubly weighted by the reviewer, who we note was in the past a member of your research group) on procedural details of the analyses obscures the major contribution of our paper. As demonstrated below, even if we use a different analytical method, the key data that stimulate this concept, which is that the porosity is critically low, will not change. We hope that it is possible to allow this observation inspired concept to be presented to our community, since we expect it to stimulate new and novel research in other fault zones.

Following your request, we have included SEM data to the manuscript. This data is a part of an unpublished PhD thesis, thus we have added that thesis' author, Dr. Risa Matsumura, as a co-author of this manuscript.

Below we have provided a point-by-point response. Line numbers are listed with respect to the manuscript with track changes on.

Best Regards,

Dr. Martina Kirilova

On behalf of co-authors: Virginia Toy, Katrina Sauer, François Renard, Klaus Gessner, Richard Wirth, Xianghui Xiao, and Risa Matsumura

Dear Authors,

Thank you for your reply to my comments. Unfortunately, it does not convince me that your porosity estimates are robust and support your interpretations sufficiently. Your descriptions are neither precise nor detailed enough to allow for a reproduction of your analysis, and I do miss evidence that supports the choices you have made in your data processing. Just a few examples to justify these statements:

What data support your claim that binary thresholding is “more than sufficient for robust porosity segmentation”?

Response: See our answer to point 1 in Dr. Gilgannon's review.

What threshold values did you use, and how were they chosen? Where they the same between all four datasets?

Response: See our answer to point 2 in Dr. Gilgannon's review.

What is the effect of the NLM filter on your porosity quantification?

Response: Non-local means filter reduces noise, and several studies have employed it (e.g. Thomson et al., 2018; Renard et al., 2019). We have now added two sentences at the beginning of section 3.3 that summarize the effect of this filter.

Are your subvolumes statistically representative?

Response: The sub-volume crops in each sample are representative. They were carefully chosen to (i) preserve the typical microstructural characteristics within a sample, and (ii) to exclude ring artifacts or big fractures (obviously induced by coring) as much as possible.

Where all of your pores labelled on the basis of face-connected pores?

Response: All pores were labelled on the basis of face-connected pores. This question was already addressed during the previous round of revisions and the information was added at line 116, but due to further revisions it is now at lines 143 and 147.

What degree of voxel connectivity did you choose to label your pores?

Response: No limit of voxel connectivity was implemented. Limits within Avizo software were introduced purely for visualization purposes as previously noted at line 147.

All of this is critical, as your entire interpretation is based on your segmented porosity data. Your reference to Menegon et al., (2015) and Gilgannon et al. (2017) is to a degree justified, both do indeed use the same thresholding technique. However, we now have significantly more sophisticated algorithms freely available, and they should be used. The significance of the choice of segmentation technique has been demonstrated in a large number of publications.

Response: See our answer to point 1 in Dr. Gilgannon's review.

On the basis of these, I am actually certain that I could analyze your data with a different set of algorithms and arrive at significantly different numbers, which, I think, highlights the principal problem.

Response: See our answer to point 1 in Dr. Gilgannon's review.

We would be interested in the opinion of the Editorial Board whether this statement is in line with the code of conduct of Solid Earth (point 3 in [https://www.solid-earth.net/policies/obligations\\_for\\_editors.html](https://www.solid-earth.net/policies/obligations_for_editors.html): "*An editor must respect the intellectual independence of authors*").

As is, I cannot recommend the paper for publication. I do encourage you to address the concerns raised above, and I would further ask you to consider the review of your revised manuscript provided by James Gilgannon.

Response: Because the second review of Dr. Gilgannon was not submitted as part of the interactive discussion process, all the authors failed to recognize the submission of this review. We now provide a response to Dr. Gilgannon's comments.

I would further ask you to include the detailed microstructural sample description that must form the basis for your interpretation of the porosity in these rocks.

Response: We have added section 3.4, lines 214-220 in section 4.2 and Figure 8.

-----//-----//-----//-----//-----//-----//-----//-----//-----//-----

Dear Editor,

Please find my general and specific comments below for my review of the revised manuscript by Kirilova et al., titled "Micro- and nano-porosity of the active Alpine Fault zone, New Zealand".

General comments

In their revised manuscript the authors have chosen to retain the manuscript largely as is. The few additions that have been made in the methods section now help the reader not make the mistake I made when first reading the initial submission.

I understand why the authors have been reluctant to change the manuscript as it is well written and has a flow that guides the reader but I do not find the answers to my last comments satisfactory in addressing the fundamental limitations of the data. The chief concern I have is that the porosity segmentation is too simplistic to allow the interpretation that follows in the discussion of a porosity and permeability gradient. In the following specific comments I have tried to clarify why I think that the authors may be over-interpreting their data and as such why I think that the authors should make room for more discussion about the limitations of the data.

To be very clear I think that the work is good and the results can be published but first there is a need for more transparency in the methodological workflow used and how it may affect any interpretations. If the authors wish to make the claims they currently make then I think these must be made more cautiously and with enough information given to allow the reader to evaluate the discussion points. As the manuscript currently stands, the results presented do not allow a gradient in porosity and permeability to be interpreted nor the further interpretation of this that variations in dissolution-precipitation must exist, which are both key discussion points of the current manuscript.

Best,

James Gilgannon

Dear Dr. Gilgannon,

We are grateful for the overall positive and thorough feedback provided here and address the remaining concerns below.

1) the porosity segmentation is too simplistic

Response: We acknowledge the efforts of the reviewer to support his views with the analysis of a synthetic case where images with known porosity are generated. These images are created with a two-step process: 1) an image of known porosity is created, 2) then this image is blurred, an effect that we consider similar to adding noise. Finally, different gray level thresholds are applied and a variability on the estimated porosity is calculated. This example illustrates very well that when the level of noise in an image is increased, a variability in the results of a segmentation technique is encountered (Andrew, 2018). In analysing our data, we proceeded in the opposite way. First, we reduced the noise in the images by applying a non-local-means filter, and then we applied a segmentation technique. This approach ensures that the differences between several segmentation techniques remain small when the level of noise in the images is small (as shown by Figure 3h of Andrew, 2018).

The main limitations of all the possible segmentation methods are data resolution, noise level, and spatial complexity of the materials of interest (e.g. Iassonov et al., 2009; Andrä et al., 2013; Bultreys et al., 2016). Furthermore, the ground-truth/real/absolute porosity is unknown in natural samples imaged with XCT (Hapca et al., 2013), unless measured independently. The thresholding method performs as well as other segmentation techniques (e.g. classification using a supervised machine learning algorithm, watershed) when the level of noise in the images is low, as demonstrated by Figure 3h of Andrew (2018). To our knowledge, there is no segmentation procedure that can be automatically applied to various kinds of samples, without the intervention of a real scientist who can adapt the segmentation procedure to the data set and even then, the estimated porosity will only be an approximation. The method we have chosen is robust and widely used in rock physics (e.g. Iassonov et al., 2009; Fousseis et al., 2014; Qi et al., 2018; Xing et al., 2018; Macente et al., 2018; 2019; Renard et al., 2019) and potential caveats on the choice of the value of the threshold have been identified in other studies (e.g. Andrä et al., 2013).

We identified porosity as the darkest phase on the analyzed synchrotron high-contrast grey-scale images. These images have less noise than data acquired in laboratory (e.g. desktop CT tomographs). In addition, porosity in these samples is represented by separated individual pores, so there were no morphological complications with respect to spatial resolution (e.g. separating fractures such as in Figure S1 in Zhao et al., 2020). Thus, it was straightforward to segment pores by binary thresholding.

More ‘complex’ segmentation methods could be applied as an exercise, similar to what was done by Andrew (2018). This exercise is out of the scope of the present article and would be a study in itself.

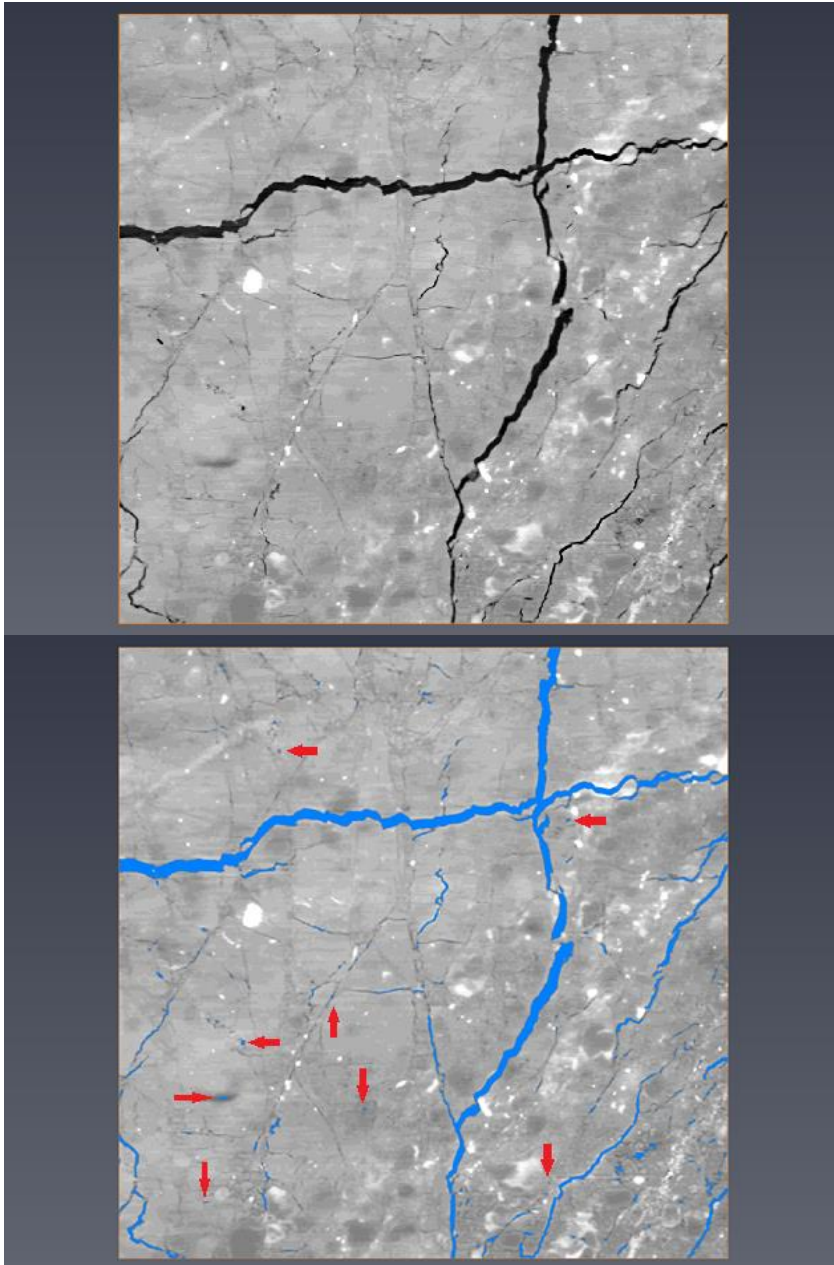
However, because we consider that the reviewer comments necessitate modification of our manuscript, we have added several paragraphs in section 3.3 to justify the choice of our segmentation technique and added two sentences in section 4.1 to estimate a variability of the porosity. We have also added some information on the variability several segmentation techniques could introduce to the estimated porosity: our preferred segmentation procedure indicates porosities in the range 0.1-0.24%. Including 20% variability due to various segmentation techniques (Andrä et al., 2013) would modify this range to 0.08-0.29%. If one considers that the level of noise in the data is low so the analysis of Andrew applies (Figure 3h, 2018), the variability between segmentation procedures would be negligible.

In summary, as we now explain in Section 3.3, different segmentation procedures will not sufficiently modify our results, and thus will not affect the discussion and central conclusions made in the manuscript.

2) **need for more transparency in the methodological workflow**

Response: We strive to be as transparent as possible about our analyses. Thus, we intend to provide the analyzed datasets in a data repository (most likely via GFZ Dataservices) to accompany the manuscript when it is published. The applied gray level threshold ranges for each sample are different because of a difference in darkness contrast between the samples. The threshold ranges applied to each samples are as follows: DFDP-1B 69\_2.54: 0 to 28; DFDP-1B 69\_2.57: 0 to 44; DFDP-1B 58\_1.9: 0 to 74; DFDP-1B 69\_2.48: 0 to 46. On the screenshots below, we display the result of the selected threshold value in sample DFDP-1B 69\_2.54, slice 363. This demonstrates that most of the porosity is due to fractures that formed during sample unloading, representative pores are shown with arrows.

Furthermore, to demonstrate the need for polynomial fitting in order to estimate total porosities in these samples we included further explanations in the text at lines 139-161 and an additional table in Supplementary material 1.



3) the results presented do not allow a gradient in porosity and permeability to be interpreted nor the further interpretation of this that variations in dissolution-precipitation must exist, which are both key discussion points of the current manuscript

Response:

Our main conclusions are based on the fact that the total porosities in these samples are extremely low. Even if different segmentation techniques would double these porosity estimates (e.g. Andrä et al., 2013), these numbers will remain very low, well under 1% total porosity. The fact that one sample contains twice the total porosity of others is an observation that deserves discussion. We have further clarified this in the manuscript in lines 289-293. Furthermore, evidence for pressure-solution process in these rocks have been documented in numerous previous studies (Sutherland et al., 2012; Toy et al., 2015;

Schleicher et al., 2015; Williams et al., 2017) and also observed on the TEM images presented in the current manuscript. Therefore, our results are sufficient to support the main conclusion. This conclusion, which is novel and innovative, is not dependent on the absolute value of the segmented porosity.

## References

- Andrä, H., Combaret, N., Dvorkin, J., Glatt, E., Han, J., Kabel, M., ... & Marsh, M. (2013). Digital rock physics benchmarks-Part I: Imaging and segmentation. *Computers & Geosciences*, 50, 25-32.
- Andrew, M., 2018, A quantified study of segmentation techniques on synthetic geological XRM and FIB-SEM images, *Computational Geosciences*, 22(6), 1503-1512.
- Bultreys, T., Boone, M. A., Boone, M. N., De Schryver, T., Masschaele, B., Van Hoorebeke, L., & Cnudde, V. (2016). Fast laboratory-based micro-computed tomography for pore-scale research: illustrative experiments and perspectives on the future. *Advances in water resources*, 95, 341-351.
- Fussei, F., Xiao, X., Schrank, C., and De Carlo, F., 2014, A brief guide to synchrotron radiation-based microtomography in (structural) geology and rock mechanics, *Journal of Structural Geology*, 65, 1-16.
- Hapca, S. M., Houston, A. N., Otten, W., & Baveye, P. C. (2013). New local thresholding method for soil images by minimizing grayscale intra-class variance. *Vadose Zone Journal*, 12(3): vzj2012.0172.
- Iassonov, P., Gebrenegus, T., & Tuller, M. (2009). Segmentation of X-ray computed tomography images of porous materials: A crucial step for characterization and quantitative analysis of pore structures. *Water resources research*, 45(9), W09415.
- Macente, A., Fussei, F., Butler, I. B., Tudisco, E., Hall, S. A., & Andò, E. (2018). 4D porosity evolution during pressure-solution of NaCl in the presence of phyllosilicates. *Earth and Planetary Science Letters*, 502, 115-125.
- Macente, A., Vanorio, T., Miller, K. J., Fussei, F., & Butler, I. B. (2019). Dynamic Evolution of Permeability in Response to Chemo-Mechanical Compaction. *Journal of Geophysical Research: Solid Earth*, 124(11), 11204-11217.
- Renard, F., McBeck, J., Cordonnier, B., Zheng, X., Kandula, N., Sanchez, J. R., ... & Fussei, F. (2019). Dynamic in situ three-dimensional imaging and digital volume correlation analysis to quantify strain localization and fracture coalescence in sandstone. *Pure and Applied Geophysics*, 176(3), 1083-1115.
- Qi, C., Wang, X., Wang, W., Liu, J., Tuo, J., & Liu, K. (2018). Three-dimensional characterization of micro-fractures in shale reservoir rocks. *Petroleum Research*, 3(3), 259-268.
- Schleicher, A. M., Sutherland, R., Townend, J., Toy, V. G., and Van Der Pluijm, B. A., 2015, Clay mineral formation and fabric development in the DFDP-1B borehole, central Alpine Fault, New Zealand, *New Zealand Journal of Geology and Geophysics*, 58(1), 13-21.
- Sutherland, R., Toy, V. G., Townend, J., Cox, S. C., Eccles, J. D., Faulkner, D. R Prior, D.J., Norris, R.J., Mariani, E., Boulton, C. and Carpenter, B.M., 2012, Drilling reveals fluid

control on architecture and rupture of the Alpine fault, New Zealand, *Geology*, 40(12), 1143-1146.

Thomson, P. R., Aituar-Zhakupova, A., & Hier-Majumder, S. (2018). Image segmentation and analysis of pore network geometry in two natural sandstones. *Frontiers in Earth Science*, 6, 58.

Toy, V. G., Boulton, C. J., Sutherland, R., Townend, J., Norris, R. J., Little, T. A., and Scott, H., 2015, Fault rock lithologies and architecture of the central Alpine fault, New Zealand, revealed by DFDP-1 drilling, *Lithosphere*, L395-1.

Williams, J. N., Toy, V. G., Smith, S. A. and Boulton, C., 2017, Fracturing, fluid-rock interaction and mineralisation during the seismic cycle along the Alpine Fault, *Journal of Structural Geology*, 103, 151-166.

Xing, T., Zhu, W., Fuisseis, F., & Lisabeth, H. (2018). Generating porosity during olivine carbonation via dissolution channels and expansion cracks. *Solid Earth*, 9(4), 879-896.

Zhao, Q., Glaser, S. D., Tisato, N., & Grasselli, G. (2020). Assessing Energy Budget of Laboratory Fault Slip Using Rotary Shear Experiments and Micro-Computed Tomography. *Geophysical Research Letters*, 47(1), e2019GL084787.



# Micro- and nano-porosity of the active Alpine Fault zone, New Zealand

Martina Kirilova<sup>1,2</sup>, Virginia Toy<sup>1,2</sup>, Katrina Sauer<sup>1</sup>, François Renard<sup>3,4</sup>, Klaus Gessner<sup>5,6</sup>, Richard Wirth<sup>7,6</sup>, and Xianghui Xiao<sup>7,8,9</sup>, [and Risa Matsumura<sup>2</sup>](#)

<sup>1</sup>[Institut für Geowissenschaften, Johannes Gutenberg Universität-Mainz, J. J. Becher Weg 21D-55128, Mainz, Germany](#)

~~Department of Geology, University of Otago, PO Box 56, Dunedin 9054, New Zealand~~

~~<sup>2</sup>[Institut für Geowissenschaften, Johannes Gutenberg Universität Mainz, J. J. Becher Weg 21D-55128, Mainz, Germany](#)~~ [Department of Geology, University of Otago, PO Box 56, Dunedin 9054, New Zealand](#)

<sup>3</sup>Department of Geosciences, The Njord Centre, University of Oslo, Oslo 0316, Norway.

<sup>4</sup>Université Grenoble Alpes, Université Savoie Mont Blanc, CNRS, IRD, IFSTTAR, ISTERRE, BP53, 38041 Grenoble, France.

<sup>5</sup>Geological Survey of Western Australia, 100 Plain Street, East Perth, WA 6004, Australia.

<sup>6</sup>[School of Earth Sciences, The University of Western Australia, 35 Stirling Highway, Crawley, WA 6009](#)

<sup>6</sup>Helmholtz-Zentrum Potsdam, GFZ, Sektion 4.3, Telegrafenberg, 14473 Potsdam, Germany

<sup>7</sup>Advanced Photon Source, Argonne National Laboratory, Lemont, IL 60439, USA

<sup>8</sup>National Synchrotron Light Source II, Brookhaven National Laboratory, Upton, NY 11973, USA

Correspondence to: Martina Kirilova ([martina.kirilova@uni-mainz.de](mailto:martina.kirilova@uni-mainz.de))

## Abstract

Porosity reduction in rocks from a fault core can cause ~~fluid overpressure~~ [elevated pore fluid pressures](#), and consequently influence the recurrence time of earthquakes. We investigated the porosity distribution in the New Zealand's Alpine Fault core in samples recovered during the first phase of the Deep Fault Drilling Project (DFDP-1B) by using two-dimensional nanoscale and three-dimensional microscale imaging. Synchrotron X-ray microtomography-derived analyses of open pore spaces show total microscale porosities in the range of 0.1\_ to 0.244%. These pores have mainly non-spherical, elongated, flat shapes and show subtle bipolar orientation. ~~Scanning and Transmission electron microscopy imaging reveals~~ [the samples' microstructural organization, where](#) ~~that~~ nanoscale pores ornament grain boundaries of the gouge material, especially clay minerals. Our data implies that: (i) [the porosity of the fault core is very small and not connected](#), (ii) the distribution of clay minerals controls the shape and orientation of the associated pores; (iii) porosity was reduced due to pressure solution processes; and (iv) ~~ii~~ mineral precipitation in fluid-filled pores can affect the mechanical behaviour of the Alpine Fault by decreasing the already critically low total porosity of the fault core, causing [elevated pore fluid pressures](#) ~~fluid overpressure~~, and/or introducing weak mineral phases, and thus lowering the overall fault frictional strength. We conclude that the current state of [very low](#) porosity in the Alpine Fault core is likely to play a key role in the initiation of the next fault rupture.

## 36 1. Introduction

37 Fault mechanics, fault structure and fluid flow properties of damaged fault rocks are intimately related (e.g. Gratier  
38 and Gueydan, 2007; Faulkner et al., 2010). Fault rupture is associated with intense brittle fracturing that enhances  
39 porosity, and thus permeability, and therefore also possible rates and directions of fluid propagation within fault  
40 zones (e.g. Girault et al., 2018). Conversely, post seismic recovery mechanisms (gouge compaction and pressure  
41 solution processes) result in reductions of porosity, permeability and fluid flow ~~propagation reductions~~ (Renard et al,  
42 2000; Faulkner et al., 2010; Sutherland et al., 2012). These processes may cause elevated pore fluid pressures within  
43 fault cores, and trigger frictional failure (e.g. Sibson, 1990; Gratier et al., 2003; [Zhu et al., 2020](#)). Therefore, the state  
44 of porosity within rocks from fault cores can play a key role in fault slip.

45 The Alpine Fault of New Zealand is late in its seismic cycle (Cochran et al., 2017), so studying it allows us to  
46 investigate pre-earthquake conditions that may influence earthquake nucleation and rupture processes. Recently,  
47 drilling operations were undertaken in this fault zone to investigate the *in situ* conditions (Sutherland et al, 2012,  
48 2017). Slug tests in the DFDP-1B borehole (Sutherland et al., 2012) and laboratory permeability measurements of  
49 core samples (Carpenter et al., 2014) indicate permeability decreases by six orders of magnitude with increasing  
50 proximity to the fault. Furthermore, Sutherland et al. (2012) documented a 0.53 MPa fluid pressure difference across  
51 the principal slip zone (PSZ) of the fault, which suggests that the fault core has significantly lower permeability than  
52 the surrounding cataclasite units. It is therefore interpreted to act as a fault seal that limits fluid circulation within its  
53 hanging wall (Sutherland et al., 2012). Permeability variations like this are closely associated with the porosity  
54 evolution of fault cores, and thus are likely to affect the fault strength and seismic properties (Sibson, 1990; Renard  
55 et al., 2000; Gratier and Gueydan, 2007).

56 In this study, we investigate the porosity distribution in rocks from the Alpine Fault core and consider the potential  
57 effects of this porosity on fault strength. We have measured open pore spaces in these rocks from X-ray computed  
58 tomography (XCT) datasets and examined pore morphology by implementing quantitative shape analyses.  
59 Lithological and microstructural characteristics of these samples were performed by ~~and~~ using scanning electron  
60 microscopy (SEM) and transmission electron microscopy (TEM).

## 61 2. Geological setting

62 New Zealand's Alpine Fault (Fig. 1a) is a major active crustal-scale structure that ruptures in a large earthquake  
63 every  $291 \pm 23$  years, the last one of which occurred in 1717 (Cochran et al., 2017). The fault is the main constituent  
64 of the oblique transform boundary between the Australian Plate and the Pacific Plate, accommodating around 75%  
65 of the relative plate motion. Ongoing dextral strike-slip at  $27 \pm 5$  mm yr<sup>-1</sup> along the fault has resulted in a total  
66 strike-separation of ~ 480 km over the last 25 Ma (Norris and Cooper, 1995, 2001; Norris and Toy, 2014). In  
67 Neogene time, a dip-slip component added to the fault motion has resulted in more than 20 km of vertical uplift of  
68 the hanging wall (Norris and Cooper, 1995, 2001; Norris and Toy, 2014). Consequently, rocks comprising the  
69 hanging wall of the fault have been exposed in various outcrops, where they can be studied in detail. The  
70 amphibolite facies Alpine Schist is the metamorphic protolith of a ~ 1 km thick mylonite zone, which has been  
71 exhumed from depth and now structurally overlies an up to 50 m thick zone of brittlely deformed cataclasites and  
72 gouges (e.g. Norris and Cooper, 1995, 2001; Norris and Toy, 2014). These rocks have been investigated in outcrops  
73 and from samples collected in three boreholes during the two phases of the Deep Fault Drilling Project (DFDP-1A,  
74 DFDP-1B and DFDP-2B; Fig. 1a) along the Alpine Fault (Sutherland et al., 2012; Toy et al., 2015; Toy et al., 2017).

75 Most of the brittle shear displacement along the fault has been accommodated within the fault core, which includes  
76 Principal Slip Zone (PSZ) gouges and cataclasite-series rocks (Toy et al., 2015). Both in surface outcrops and drill  
77 core samples, the Alpine Fault manifests as a thin (5 to 20 cm thick) gouge zone with a predominantly random fabric  
78 of clay-rich material (Toy et al., 2015; Schuck et al., 2020). This cohesive but uncemented layer has a significantly  
79 finer-grain size significantly finer than the surrounding cataclasite units, which shows that the material was reworked  
80 only within this layer, most probably as a result of ultra-comminution due to multiple shear events under brittle

81 conditions (Boulton et al., 2012; Toy et al., 2015). The local presence of authigenic smectite clays (Schleicher et al.,  
82 2015) and calcite and/or chlorite mineralization within sealed fractures and in the gouge matrix (Williams et al.,  
83 2017) indicate that mineral reactions are restricted to an alteration zone within the fault core (Sutherland et al., 2012;  
84 Schuck et al., 2020). The Alpine Fault core has been interpreted to have formed during a cyclical history of  
85 mineralization, shear, and fragmentation (Toy et al., 2015). In addition, in the DFDP-1B borehole (Fig. 1b,  
86 Sutherland et al., 2012) fault gouges occur at two distinct depths: 128.1 m (PSZ-1) and 143.85 m (PSZ-2), which  
87 shows that the slip was not localized within a single gouge layer (Toy et al., 2015).

### 88 3. Sample description and analytical methods

#### 89 3.1 Samples

90 Porosity analyses were performed on four samples representing PSZ gouges and cataclasites of the Alpine Fault  
91 core, which were recovered from the DFDP-1B borehole (Fig. 1b, c; Sutherland et al., 2012). These are DFDP-1B  
92 58\_1.9, DFDP-1B 69\_2.48, DFDP-1B 69\_2.54 and DFDP-1B 69\_2.57. Sample nomenclature includes drill core run  
93 number, section number, and centimeters measured from the top of each section. These samples were recovered  
94 from drilled depth of 126.94 m, 143.82 m, 143.88 m and 143.91 m, respectively.

95 Detailed lithological and microstructural descriptions of the DFDP-1B drill core were carried out simultaneously  
96 with, and after the drilling operations by the DFDP-1 Science Team, and these data were later summarized by Toy et  
97 al. (2015). Samples DFDP-1B 58\_1.9 and DFDP-1B 69\_2.48 belong to foliated cataclasite units (Fig. 1b, c; Toy et  
98 al., 2015). ~~These were~~ described as ultracataclasites with gouge-filled shear zoness located above PSZ-1 and PSZ-2  
99 respectively. Sample DFDP-1B 69\_2.54 represents the gouge layer that defines PSZ-2, whereas sample DFDP-1B  
100 69\_2.57 is composed of brown ultracataclasites that belong to the lower cataclasite unit (Fig. 1b, c; Toy et al., 2015).

101

#### 102 3.2 X-ray computed tomography (XCT)

103 We imaged the samples using X-ray absorption tomography, where the signal intensity depends on how electron  
104 density and bulk density attenuate a monochromatic X-ray along its path through the material (e.g. Füsseis et al.  
105 2014). We acquired the X-ray microtomography data for this study at the 2-BM beamline of the Advanced Photon  
106 Source, Argonne National Laboratories USA in December 2012. The non-cylindrical samples of ~7 mm height and  
107 ~ 4 mm diameter were mostly drilled parallel to the foliation, and mounted on a rotary stage, and imaged with a  
108 beam energy of 22.50 keV. A charge-couple device camera collected images at 0.25° rotation steps over 180° at. A-  
109 sample-detector distance of 70 mm and yielded a field-of-view of 2.81 mm. The voxel size (i.e. spatial sampling)  
110 was 1.3 μm and the spatial resolution was likely in the ranged between from two and to three times the voxel size. We  
111 have reconstructed the datasets with a filtered back-projection parallel beam reconstruction into 32-bit gray level  
112 volumes consisting of 2083-2048 \* 2083-2048 \* 2083-2048 voxels using X-TRACT (Gureyev et al., 2011).

#### 113 3.3 Analyses of XCT datasets

114 Data analyses and image processing were performed using the commercial software package Avizo 9.1™ (Fig. 2).  
115 Initially, the datasets were rescaled to 8-bit grey scale volumes for enhanced computer performance. In addition,  
116 small volumes of interest were cropped from the whole volume before a non-local means filter was applied to  
117 reduce noise (Buades et al., 2005). For each voxel, this filter compares the value of this voxel with all neighboring  
118 voxels in a given search window. A similarity between the neighbors determines a correction applied to each voxel  
119 (e.g. Thomson et al., 2018).

120 -On the filtered gray-scale images, pores were identified as disconnected materials of as porosity was identified as  
121 the darkest phase-grey-scale range (Fig. 2a).- The corresponding gray-scale values were thresholded, and the datasets  
122 were converted into binary form. This step is called segmentation. Several segmentation techniques exist, from

123 thresholding at a given gray scale value (e.g. Ianossov et al., 2009; Andrewä et al., 2013) to deep learning algorithms  
124 (Ma et al., 2020). ~~The choice of one~~It is up to the user to choose the segmentation technique ~~or another~~that is most  
125 appropriate to analyze a given dataset ~~is user dependent~~. To our knowledge, no single segmentation technique can  
126 be generalized and universally used independently of the nature of the samples. In the present study, we have chosen  
127 a simple segmentation technique by applying a threshold to the gray scale images to separate the void space from the  
128 solid. This technique has been used in many studies in the last two decades ~~since the 2000's~~ to characterize porosity  
129 in rocks, including some very ~~and was applied in~~ recent studies in rock physics (Macente et al., 2019; Renard et al.,  
130 2019). ~~The variability on~~†The segmented porosity volume depends strongly on the choice of the threshold and some  
131 studies have ~~reported~~demonstrated that the final porosity estimated by different segmentation methods ~~could~~can  
132 vary ~~within an error of~~by 20% (Andrä et al., 2013). ~~A recent study has shown that~~.However, when the level of noise  
133 in the data is low, the differences in porosities estimated ~~between various~~by different segmentation techniques is  
134 negligible (Figure 3h in Andrew, 2018). Our data ~~have been~~were acquired at a synchrotron where the parallel beam  
135 and high photon flux ensured a low level of the noise in the images. In addition, ~~the~~application of a non-local-means  
136 filter applied to our data ~~has~~reduced the noise level. For these reasons, we consider that ~~the~~it was robust to apply  
137 ~~choice of~~ a simple thresholding technique is robust ~~for~~to this dataset ~~and~~but acknowledge that the porosity values we  
138 ~~give~~estimate later ~~could have a small error that cannot be estimated because~~differ by <20% from the ground truth~~the~~  
139 'true' porosity of the rock is not known, as discussed in (cf. Andrä et al., 2013; Hapca et al., (2013)).

140 However, ~~our segmentation procedure~~this threshold range also captured cracks within a sample, which are likely to  
141 result from depressurization during core recovery (Fig. 2b). ~~To omit the cracks, we utilized the morphological~~  
142 operation 'connected components' available in the software Avizo 9.1, which allows volumes larger than selected  
143 number of connected voxels to be excluded from the binary label images. To each sample we applied upper limits of  
144 20 (43.94  $\mu\text{m}^3$ ), 50 (109.85  $\mu\text{m}^3$ ), 100 (219.7  $\mu\text{m}^3$ ) and 200 (439.4  $\mu\text{m}^3$ ) face connected voxels. Total porosities  
145 estimates based on these operations are presented as percentages of the sample volume in Supplementary material 1.  
146 Unfortunately, this methodology results in either loss of larger pores or inclusion of small cracks depending on the  
147 implemented limit of connected components, and thus the calculated porosities include significant bias. Therefore,  
148 the operation 'connected components' was used only for visualization purposes, and clusters of 200 face connected  
149 voxels were created to show the 3D volumes of segmented pore spaces (Fig. 2c)

150 ~~To omit the cracks, thresholded components with volumes larger than the volume of 200 connected voxels (439.4~~  
151  $\mu\text{m}^3$ ) were excluded from the binary label images by using the morphological operation 'connected components'  
152 built available in the software Avizo 9.1. Clusters of connected components were then created to visualize 3D  
153 volumes of segmented pore spaces (Fig. 2c).

154 ~~Unfortunately, this methodology results in either loss of larger pores or inclusion of small cracks depending on the~~  
155 ~~implemented limit of connected components, and thus calculating total~~calculated porosities includes significant bias.  
156 ~~Instead~~Instead, the volumes ~~and shape characteristics~~ of segmented materials (including cracks ~~i.e. without any data~~  
157 ~~limitation~~) were exported from Avizo software in numerical format, and volume distributions within a sample were  
158 plotted on a logarithmic scale ~~in Matlab~~(Fig. 3). Data up to a specific volume size were fit to a polynomial curve,  
159 and then the curve was extrapolated to the X-axis intercept, which is the expected maximum pore size (Fig. 3). ~~For~~  
160 ~~each sample the~~†Total porosities ~~were~~as then estimated by integrating the curve, which excludes all volumes on  
161 the right side of the curve. Total porosities are presented as a percentage of the whole sample volume (Fig. 3). The  
162 implemented equations are ~~presented~~given in Supplementary material 1.

163

164 Pore shapes were analyzed on bivariate histograms ~~plotted on Matlab~~by using the numerical pore characteristics,  
165 ~~previously extracted from Avizo software~~. Only pore volumes between 21.97  $\mu\text{m}^3$  (10 voxels) and 878.8  $\mu\text{m}^3$  (400  
166 voxels) were included to avoid bias in the data due to insufficient voxel count and presence of cracks, respectively.  
167 ~~Individual pores in our dataset are separated (Fig. 2c).~~For each pore,†The covariance matrix of ~~the volume~~each pore  
168 was calculated, and the three eigenvalues of this covariance matrix were extracted. These three values correspond to

169 the three main orthogonal directions in each pore (i.e. the longest, medium and shortest axes) and we use them as  
170 proxies to describe pore geometry. Thus, their amplitudes provide information on the spatial extension of ~~the a given~~  
171 pore and its shape. The ratio between the medium and largest eigenvalues of each pore defines its elongation (Fig.  
172 4), the ratio between the smallest ~~to and~~ the largest ~~eigenvalues defines~~ its sphericity (Fig. 5), and the ratio of the  
173 smallest ~~to and~~ the medium ~~eigenvalues defines~~ its flatness (Fig. 6).

174 The angles  $\theta$  and  $\varphi$  that describe the orientation of the longest ~~eigenvalue (i.e. axis)~~ of each pore with respect to the  
175 ~~main global orthogonal axis system~~ of the 3D scan were calculated. These angles were translated into trend and  
176 plunge and then plotted on a lower hemisphere equal area stereographic projection with a probability density  
177 contour to display the distribution of pore unit orientations (Fig. 7).

### 178 **3.4 Scanning electron microscopy (SEM)**

179 ~~SEM images were collected on Zeiss Sigma-FF-SEM at the University of Otago's Centre for Electron Microscopy.~~  
180 ~~The SEM was operated at a working distance of 8.5 mm, an accelerating voltage of 10 keV and a 120  $\mu\text{m}$  aperture~~  
181 ~~with dwell time of 100 $\mu\text{s}$ . EDS maps were created by using Aztec Software ([https://www.oxford-](https://www.oxford-instruments.com/products/microanalysis/energy-dispersive-x-ray-systems-eds-edx/eds-for-sem/eds-software-aztec)~~  
182 ~~[instruments.com/products/microanalysis/energy-dispersive-x-ray-systems-eds-edx/eds-for-sem/eds-software-aztec](https://www.oxford-instruments.com/products/microanalysis/energy-dispersive-x-ray-systems-eds-edx/eds-for-sem/eds-software-aztec)).~~

183

### 184 **3.5 Transmission electron microscopy (TEM)**

185 ~~High resolution~~ TEM images were collected on a FEI Tecnai G2 F20 X-Twin transmission electron microscope,  
186 located at the German Research Centre for Geosciences (GFZ), Potsdam, Germany (~~Fig. 8~~ Fig. 9). The instrument is  
187 equipped with field-emission gun (FEG) electron source and high-angle annular dark-field (HAADF) Detector.  
188 Images were collected from samples placed on a Gatan double-tilt holder at ~~an accelerating voltage of 200kV. These~~  
189 ~~TEM samples were preparation was performed with~~by focused ion beam (FIB) milling at GFZ Potsdam using a  
190 HELIOS system operated at ~~an accelerating voltage of 30 kV.~~

## 191 **3.4 Results**

### 192 **4.1 XCT-derived characteristics of porosity**

193 All samples contain low total porosities, ranging from 0.1% to 0.24% (Fig. 3). ~~If different segmentation techniques~~  
194 ~~were applied, a variability between in the range that Andrew (2018) demonstrated is reasonable, from nearly nearly~~  
195 ~~0% to (e.g. Figure 3h in Andrew, 2018) to 20%. (Andrä et al., 2013) would correspond to porosities between 0.08%~~  
196 ~~and 0.29% in our samples. However, it should can~~ be noted that the lower cataclasite sample (DFDP-1B 69\_2.57)  
197 has twice as much pore space (Fig. 3d) as any of the other samples. The characterized pore ~~size volume~~ distributions  
198 range over almost three orders of magnitude ~~for all samples (Fig. 3). Furthermore, the expected maximum pore size~~  
199 ~~volume was estimated to be largest in the PSZ-2 sample (DFDP-1B 69\_2.54), reaching 862  $\mu\text{m}^3$  (Fig. 3c). All pores~~  
200 ~~are disconnected to each others.~~

201 In all samples, shape analyses of pores with volumes between 21.97  $\mu\text{m}^3$  (10 voxels) and 878.8  $\mu\text{m}^3$  (400 voxels)  
202 demonstrate predominantly elongated (Fig. 4), non-spherical (Fig. 5) and flat pore shapes (Fig. 6). This is  
203 particularly pronounced for the smaller pore volumes. The number of elongated pores per sample ~~is~~  
204 ~~increasing increases~~ in the upper foliated cataclasites (Fig. 4a and b) with increasing proximity to PSZ-2, where most  
205 elongated pores occur (Fig. 4c). Conversely, the lower cataclasite sample demonstrates proportionally fewer  
206 elongated pores within the sample (Fig. 4d). The degree of sphericity is uniform for all samples, and pores appear as  
207 mainly non-spherical (Fig. 5). Few isolated spherical pores are manifested only by small pore volumes (Fig. 5). A  
208 trend of increasing the number of flat pores is observed with increasing sample depth (Fig. 6), and most flat pores  
209 are detected in the lower cataclasite (Fig. 6d).

210 The orientations of the individual pore units show two distinctive peaks with opposite vergence, defining bipolar  
211 distributions of pore orientations (Fig. 7). The observed bipolarity is subtle in samples DFDP-1B 58\_1.9 (Fig. 7a)  
212 and DFDP-1B 69\_2.48 (Fig. 7b), and more obvious in samples DFDP-1B 69\_2.54 (Fig. 7c) and DFDP-1B 69\_2.57  
213 (Fig. 7d).

## 214 4.2 Microstructural characteristics of porosity

215 To demonstrate the microstructural arrangement of the cataclasites, we show representative SEM images from  
216 sample DFDP-1B 69\_248 (Fig. 8), previously described as a ‘lower foliated cataclasite’ by Toy et al., 2015. SEM  
217 images presented here reveal rounded to sub-rounded crystalline clasts up to 100 µm in diameter (Fig. 8a, b), which  
218 consist of ~50 % plagioclase, ~40 % K-feldspar, and ~10 % quartz and are elongated at angles of 0-30° to the  
219 foliation. The surrounding matrix material is composed of finer grains (< 30 µm in diameter) of white micas,  
220 chlorite, K-feldspar, calcite and Ti-oxide (Fig. 8c). Numerous quartz clasts contain microfractures, filled by calcite  
221 and/or chlorite.

222 TEM characterization of the gouge material from PSZ-2 (sample DFDP-1B 69\_2.54) reveals that the Alpine Fault  
223 gouges ~~have composition, are composed of comprising~~ angular quartz and/or feldspar fragments (~200 nm in size),  
224 wrapped by smaller phyllosilicates (< 100 nm long). This random fabric is ornamented by nanoscale pores (< 50  
225 nm), distributed along all grain and phase boundaries, but especially abundant along within/around clay minerals  
226 (Fig. 8 Fig. 9a).

227 The gouge material also demonstrates phyllosilicate-rich areas, defined by an increase in the clay/clast ratio. In these  
228 zones, fine (< 100 nm long) and coarser (few µm long) clay grains coexist and are aligned in wavy fabric that  
229 surrounds sporadic protolith fragments (Fig. 8 Fig. 9b). Pore spaces are again distributed along the boundaries of the  
230 constituent mineral grains but some of them are larger (~0.5 µm) with and thin ellipsoidal or elongated shapes (Fig.  
231 8 Fig. 9b, c). These pores are commonly associated with inter-clay layer porosity. Large size pores are also observed  
232 along quartz-feldspar grain phase boundaries. These latter, where pores are associated with multiple grains and  
233 occasionally disrupt grain the boundaries, thus were labelled as cracks along boundaries of quartz and/or feldspar  
234 grains (i.e. fracture porosity; Fig. 8 Fig. 9d).

## 235 5 Discussion

### 236 5.1 Characteristics of porosity within the Alpine Fault core

237 Porosity analyses of samples from, or in close proximity to the two PSZs encountered in the DFDP-1B drill core  
238 reveal total pore volumes between ~0.1% and 0.24% (Fig. 3). These values are significantly lower than the porosity  
239 estimates from other active faults in the world, such as: 0.2 to 5.7% total porosity in the core of the Nojima Fault,  
240 Japan (Surma et al., 2003) and 0 to 18% in the San Andreas Fault core (Blackburn et al., 2009). The Alpine Fault  
241 core contains total pore space volumes, comparable only with the lower porosities in these previous studies. It  
242 should be noted that the smallest pore spaces captured in the XCT datasets are 1.3 µm in size due to resolution  
243 acquisition constraints, whereas nanoscale porosity was identified on the TEM images. Therefore, the estimated total  
244 porosities from XCT data represent only minimum values of the open pore spaces in the Alpine Fault core.  
245 ~~However, the addition of nanoscale porosity volumes is unlikely to dramatically affect the final total porosity of~~  
246 ~~these rocks because they comprise a very small total volume.~~

247  
248 TEM images presented here mainly focus on nano-scale materials (Fig. 8 Fig. 9a, c, d) but were also used to describe  
249 the distribution of micro-porosity in these rocks (Figure 8 Figure 9b). The pores visible on grain and phase  
250 boundaries in On figure 8 figure 9b pores have similar sizes comparable to the small range of pores segmented on  
251 XCT images (> 1.3 µm in diameter), and thus we conclude that this is the typical habit of both nano- and micro-

252 pores within the Alpine Fault core ~~are distributed on grain and phase boundaries, especially of clay minerals (Fig.~~  
253 ~~8Fig. 9)~~. In addition, both quantitative micro-porosity shape analyses (Fig. 4, 5 and 6) and nano-pores identified on  
254 TEM images (~~Fig. 8Fig. 9~~) reveal that a significant population of pores are predominantly non-spherical with  
255 elongated, flat shapes. We attribute this observation to the tendency of these pores to ornament clay minerals where  
256 pores are ~~attained distributed~~ and elongated along their (001) planes (~~Fig. 8Fig. 9b, c and d~~).

257 Foliation in the upper cataclasites is defined by clay-sized phyllosilicates, that become more abundant with  
258 proximity to the PSZ (Toy et al., 2015), where ~~a~~ weak clay fabric is developed (Schleicher et al., 2015). This gradual  
259 enrichment in clay minerals coincides with the subtle development of bipolar distributions of pore orientations with  
260 increasing sample depth (Fig. 7). This observation and the fact that pores are mainly ~~attained distributed~~ along grain  
261 boundaries of clays (~~Fig. 8Fig. 9~~) suggest that the distribution of clay minerals also controls pore orientations within  
262 the Alpine Fault core. Previously, the phyllosilicate foliation in the Alpine Fault cataclasites has been used to define  
263 shear direction (Toy et al., 2015). Thus, we speculate that pore orientations in these rocks are also systematically  
264 related to the kinematic framework of the shear zone. If these pores represent remnants of fluid channels, their  
265 spatial orientation is likely to reflect the fluid flow directions during deformation. To address this possibility more  
266 data for systematic analyses of pore orientations are needed.

## 267 5.2 Porosity reduction within the Alpine Fault core

268 ~~The comparatively lower porosity estimates of the Alpine Fault core than other active faults (e.g. the Nojima Fault,~~  
269 ~~Surma et al., 2003, and the San Andreas Fault, Blackburn et al., 2009) could~~ ~~an~~ be attributed to the fact that the  
270 ~~Alpine Fault is late in its c. 300 year seismic cycle and the last seismic event occurred in 1717– (Cochran et al.,~~  
271 ~~2017). Thus, We propose that the fault has almost completely sealed.~~ Porosity of ~~the~~ fault cores is ~~considered~~  
272 ~~widely thought believed~~ to evolve during the seismic cycle, ~~when since~~ fault rupture can cause ~~porosity porosities to~~  
273 increase up to 10% (Marone et al., 1990), and ~~the conse~~ subsequent healing ~~by various~~ mechanisms, ~~(such as~~  
274 ~~mechanical compaction of the fault gouge and/or elimination of pore spaces within the fault core due to pressure~~  
275 ~~solution processes); lead causesto~~ porosity ~~to~~ decrease over time ~~due to mechanical compaction of the fault gouge~~  
276 ~~and/or elimination of pore spaces within the fault core due to pressure solution processes~~ (Sibson, 1990; Renard et  
277 al., 2000; Faulkner et al., 2010). ~~SEM/TEM~~ data presented here show ~~that fine--grained chlorite and muscovite~~  
278 ~~grains aetformed as a cement in the cataclastic matrix (Fig. 8c). Our TEM data reveals the~~ abundance of newly  
279 precipitated authigenic clays, wrapped around coarser clay minerals (~~Fig. 8Fig. 9b~~). Furthermore, delicate clay  
280 minerals form fringe structures (~~Fig. 8Fig. 9a~~), and strain shadows (~~Fig. 8Fig. 9c~~) around larger quartz-feldspar  
281 grains. These microstructural observations demonstrate that pressure solution processes operated within these rocks  
282 (~~Toy et al., 2015~~).

283 Evidence for pressure solution processes has been previously documented in all units, comprising the Alpine Fault  
284 core (Toy et al., 2015). Abundant precipitation of alteration minerals (Sutherland et al., 2012), calcite filled  
285 intragranular and cross-cutting veins (Williams et al., 2017), and the occurrence of newly formed smectite clays  
286 (Schleicher et al., 2015) indicate extensive fluid-rock reactions. In addition, anastomosing networks of opaque  
287 minerals (such as graphite; Kirilova et al., 2017), which define foliation in the upper cataclasites (Toy et al., 2015),  
288 have been interpreted to be concentrated by pressure solution processes during aseismic creep (Toy et al., 2015;  
289 Gratier et al., 2011). The petrological characteristics of the Alpine Fault core lithologies ~~identify indicate that~~  
290 solution transfer ~~mechanisms likely wasere likely~~ the dominant mechanism for pore closure within these rocks.

291 ~~Porosity estimates presented here are so low that presumably negligible variations in between samples can represent~~  
292 ~~significant gradients in porosity. For example, the increase of total porosity in sample DFDP-1B 69-2.57 with only~~  
293 ~~0.14%, manifests as twice as many open pore spaces in comparison to the rest of the analyzed samples (Fig. 3). In~~  
294 ~~addition, this is the only footwall sample analyzed here and as aforementioned already mentioned in section 3.1 does~~  
295 ~~not contain any gouge material.~~ Post-rupture porosity reduction is known to operate three to four times faster within  
296 fine-grained fault gouges than in coarser-grained cataclasites (Walder and Nur, 1984; Sleep and Blanpied, 1992;  
297 Renard et al., 2000); which may explain the ~~porosity differences demonstrated above, differences in total porosity~~

298 ~~between the gouge containing samples and the footwall ultracataclasite—DFDP 1B 69 2.57 (Fig. 3).~~ Furthermore,  
299 previous studies documented less carbonate and phyllosilicate filling of cracks in the Alpine Fault footwall  
300 cataclasites ~~as compared to~~ than in the hanging wall cataclasites (Sutherland et al., 2012; Toy et al., 2015),  
301 suggesting more reactive fluids are present and isolated within ~~g~~ the hanging wall of the Alpine Fault. Thus, more  
302 intense dissolution-precipitation processes took place in the fault's hanging wall, which very likely resulted in more  
303 efficient porosity reduction, as demonstrated by our porosity estimates (Fig. 3).

304 ~~As aforementioned, porosity reduction is known to increase with time after an earthquake event due to post rupture~~  
305 ~~healing mechanisms (Sibson, 1990; Renard et al., 2000; Faulkner et al., 2010). Thus, the comparatively lower~~  
306 ~~porosity estimates of the Alpine Fault core than other active faults (e.g. the Nojima Fault, Surma et al., 2003, and the~~  
307 ~~San Andreas Fault, Blackburn et al., 2009) can be attributed to the fact that the Alpine Fault is late in its seismic~~  
308 ~~cycle (Cochran et al., 2017).~~

### 309 5.3 Effects of porosity on the Alpine Fault strength

310 ~~The extremely~~ Very low porosity estimates are presented here (Fig. 3). ~~are consistent with the~~ Very low  
311 permeabilities of  $10^{-18}$  m<sup>2</sup> ~~were also~~ measured experimentally in clay-rich cataclasites and gouges from the Alpine  
312 Fault zone (Carpenter et al., 2014). In addition, the documented difference of total porosities between the hanging  
313 wall and footwall samples (Fig. 3) ~~implies may be interpreted as to reflect~~ different intensities ~~iesy~~ of pressure solution  
314 processes, and thus ~~compartmented compartmentalisation compartmentalization of percolating fluids propagation.~~  
315 Our porosity data ~~thus provide independent verification is comparable with of show a spatial trend similar to the~~  
316 permeability measurements ~~in that study of~~ (Carpenter et al., (2014)). ~~This observation and yields~~ increased  
317 confidence in ~~their the~~ interpretation of Carpenter et al. (2014) of a permeability gradient with distance from the  
318 PSZ, which itself acts as a hydraulic seal (Sutherland, et al., 2012). The existence of such a barrier to flow is  
319 characteristic for faults undergoing creep and locked faults (Rice, 1992; Labaume et al., 1997; Wiersberg and  
320 Erzinger, 2008). However, much higher permeabilities in the surrounding damaged rocks (Carpenter et al., 2014)  
321 allow fast propagation of fluids within them and can cause localization of high fluid pressures on one side or the  
322 other of a hydraulic seal (Sibson, 1990). Such fluid pressures can enhance gouge compaction and pressure solution  
323 processes ~~within the fault core~~, which will eventually introduce zones of weakness and thus may trigger fault slip  
324 (Faulkner et al., 2010).

325 Previous studies and the observations presented here show that fluids were present in the Alpine Fault rocks. Fluid-  
326 filled pores represent a favorable environment for mineral precipitation, which can affect the fault strength in two  
327 ways: (i) Very small decrease of these critically low total porosities due to mineral precipitation would cause fluid  
328 pressurization, ~~which is~~ a well-known fault weakening mechanism ~~described by (Byerlee, (1990;) and Sibson,~~  
329 ~~(1990); H; however, this pressure increase will could be slightly offset by inclusion of fluids into new hydrous~~  
330 ~~minerals;~~ (ii) deposition of frictionally weak phases (such as clay minerals and graphite), especially if they decorate  
331 grain contacts and/or form interlinked weak layers, would lower the overall frictional strength (Rutter et al., 1976;  
332 Niemeijer et al., 2010).

333 ~~Precipitation of~~ authigenic clay minerals ~~was were~~ identified ~~on in~~ our TEM data (~~Fig. 8~~ Fig. 9) and also  
334 documented by previous studies (Schleicher et al., 2015). As well as having low frictional strengths (Moore and  
335 Lockner, 2004), clay minerals may also contribute to the formation of an impermeable seal if they form an aligned  
336 fabric, ~~and thus can which can~~ enhance the likelihood of fluid-pressurization in the fault rocks (Rice, 1992; Faulkner  
337 et al., 2010). In addition, graphite, ~~which was previously documented in these rocks by previous studies (Kirilova et.~~  
338 ~~al., 2017),~~ may effectively weaken the fault due to mechanical smearing (Rutter et al., 2013) and/or localized  
339 precipitation within strained areas (Upton and Craw, 2008). Such graphite precipitation within shear surfaces was  
340 previously documented by Kirilova et al. (2017).

341 In summary, the presence of trapped fluids in the low porosity rocks of the Alpine Fault core possibly controls the  
342 mechanical behavior of the fault and could be responsible for future rupture initiation due to fluid pressurization



343 and/or precipitation of weak mineral phases. This hypothesis is further supported by an experimental study showing  
344 that the DFDP-1 gouges are frictionally strong in the absence of elevated fluid pressure (Boulton et al., 2014).

## 345 **6 Conclusions**

346 Analyses of XCT-datasets and TEM images of borehole samples from the core of the Alpine Fault reveal micro- and  
347 nanoscale pores, distributed along grain boundaries of the constituent mineral phases, especially clay minerals. The  
348 tendency of these pores to ornament clays defines their predominantly non-spherical, elongated, flat shapes and the  
349 bipolar distribution of pore orientations. The documented extremely low total porosities (~~from in the range 0.1 to~~  
350 0.24 %) in these rocks suggest effective porosity reduction and fault healing. Microstructural observations presented  
351 here and documented in previous studies indicate that pressure solution processes were the dominant healing  
352 mechanism, and that fluids were present in these rocks. Therefore, fluid-filled pores may be places where ~~fluid~~  
353 ~~overpressure~~ elevated pore fluid pressures develop, due to further mineral precipitation that decreases the already  
354 critically low total porosities. ~~Alternatively, they these pores~~ may also facilitate the deposition of weak mineral  
355 phases (such as clay minerals and graphite) that may very effectively weaken the fault. We conclude that the current  
356 state of the fault core porosity is possibly a controlling factor on the mechanical behaviour of the Alpine Fault and  
357 will likely play a key role in the initiation of the next fault rupture.

### 358 **Data availability.**

359 Matlab ~~code~~ scripts and numerical data of pore volumes can be found in Supplementary material 1.

### 360 **Authors contribution**

361 Kirilova reconstructed, processed, and analysed the XCT datasets presented here, interpreted the TEM data and  
362 prepared the manuscript. Most of this work was performed during Kirilova's PhD under the academic guidance of  
363 Toy. Toy and Gessner collected the XCT data with technical support by Xiao. Renard and Sauer contributed with  
364 valuable discussion about XCT data analyses and edited the manuscript. Wirth enabled TEM data acquisition and  
365 provided his expertise on TEM data interpretation. Matsumura collected and analyzed the presented SEM data. The  
366 final version of this manuscript benefits from collective intellectual input.

### 367 **Competing interests**

368 The authors declare that they have no conflict of interest.

### 369 **Acknowledgments**

370 We gratefully acknowledge funding from the Advances Photon Source (GUP 31177). This research used resources  
371 of the Advanced Photon Source, a U.S. Department of Energy (DOE) Office of Science User Facility operated for  
372 the DOE Office of Science by Argonne National Laboratory under Contract No. DE-AC02-06CH11357. Avizo  
373 workstation was built at the University of Otago with financial support provided by Nvidia Corporation, Royal  
374 Society of New Zealand's Rutherford fellowships (16-UOO-001), the Ministry of Business and Innovation's  
375 Endeavor Fund (C05X1605/GNS-MBIE00056), and a subcontract to the Tectonics and Structure of Zealandia  
376 Program at GNS Science (GNS-DCF00020). Publishing bursary funding provided by the University of Otago is  
377 greatly appreciated. We thank Sherry Mayo for helping with the reconstruction process of XCT data and Andrew  
378 Squelch for providing use of the Avizo workstation, located at CSIRO, Perth, Australia during the initial data  
379 analyses. Special thanks to Reed Debaets for assistance with the development of Matlab code. Klaus Gessner  
380 publishes with permission of the Executive Director, Geological Survey of Western Australia.

381 **References**

- 382 [Andrä, H., Combaret, N., Dvorkin, J., Glatt, E., Han, J., Kabel, M., Keehmd, Y., Krzikallac, F., Leed, M.,](#)  
383 [Madonnae, C., Marshb, M., Mukerjic, T., Saengere, E. H., Sainf, R., Saxenac, N., Rickera, S., Wiegmann, A., and](#)  
384 [Zhanf, X., ... & Marsh, M., 2013, Digital rock physics benchmarks—Part I: Imaging and segmentation. \*Computers\*](#)  
385 [& \*Geosciences\*, 50, 25-32.](#)
- 386 [Andrew, M., 2018, A quantified study of segmentation techniques on synthetic geological XRM and FIB-SEM](#)  
387 [images. \*Computational Geosciences\*, 22\(6\), 1503-1512.](#)
- 388 Berryman, K. R., Cochran, U. A., Clark, K. J., Biasi, G. P., Langridge, R. M., and Villamor, P., 2012, Major  
389 earthquakes occur regularly on an isolated plate boundary fault, *Science*, 336(6089), 1690-1693.
- 390 Blackburn, E. D., Hadizadeh, J., and Babaie, H. A., 2009, A microstructural study of SAFOD gouge from actively  
391 creeping San Andreas Fault zone: Implications for shear localization models, *in* AGU Fall Meeting Abstracts.
- 392 Buades, A., Coll, B. and Morel, J. M., 2005, A non-local algorithm for image denoising, *in* Computer Vision and  
393 Pattern Recognition, IEEE Computer Society Conference, Vol. 2, pp. 60-65.
- 394 Boulton, C., Carpenter, B. M., Toy, V., and Marone, C., 2012, Physical properties of surface outcrop cataclastic  
395 fault rocks, Alpine Fault, New Zealand, *Geochemistry, Geophysics, Geosystems*, 13, Q01018,  
396 doi:10.1029/2011GC003872.
- 397 Boulton, C., Moore, D. E., Lockner, D. A., Toy, V. G., Townend, J., and Sutherland, R., 2014, Frictional properties  
398 of exhumed fault gouges in DFDP-1 cores, Alpine Fault, New Zealand, *Geophysical Research Letters*, 41(2), 356-  
399 362.
- 400 Byerlee, J., 1990, Friction, overpressure and fault normal compression, *Geophysical Research Letters*, 17(12), 2109-  
401 2112.
- 402 Carpenter, B. M., Kitajima, H., Sutherland, R., Townend, J., Toy, V. G., and Saffer, D. M., 2014, Hydraulic and  
403 acoustic properties of the active Alpine Fault, New Zealand: Laboratory measurements on DFDP-1 drill core, *Earth*  
404 *and Planetary Science Letters*, 390, 45-51.
- 405 Cochran, U. A., Clark, K. J., Howarth, J. D., Biasi, G. P., Langridge, R. M., Villamor, P., ---[Berryman, K. R.](#), and  
406 Vandergoes, M. J., 2017, A plate boundary earthquake record from a wetland adjacent to the Alpine fault in New  
407 Zealand refines hazard estimates, *Earth and Planetary Science Letters*, 464, 175-188.
- 408 Faulkner, D. R., Jackson, C. A. L., Lunn, R. J., Schlische, R. W., Shipton, Z. K., Wibberley, C. A. J., and Withjack,  
409 M. O., 2010, A review of recent developments concerning the structure, mechanics and fluid flow properties of fault  
410 zones, *Journal of Structural Geology*, 32(11), 1557-1575.
- 411 Fusseis, F., Xiao, X., Schrank, C., and De Carlo, F., 2014, A brief guide to synchrotron radiation-based  
412 microtomography in (structural) geology and rock mechanics, *Journal of Structural Geology*, 65, 1-16.
- 413 Girault, F., Adhikari, L. B., France-Lanord, C., Agrinier, P., Koirala, B. P., Bhattarai, M., and Perrier, F., 2018,  
414 Persistent CO<sub>2</sub> emissions and hydrothermal unrest following the 2015 earthquake in Nepal, *Nature*  
415 *Communications*, 9(1), 2956.
- 416 Gratier, J.-P., Favreau, P., and Renard, F., 2003, Modelling fluid transfer along California faults when integrating  
417 pressure solution crack sealing and compaction processes, *Journal of Geophysical Research*, 108, 2104,  
418 doi:10.1029/2001JB000380, B2.

- 419 Gratier, J. P., 2011, Fault permeability and strength evolution related to fracturing and healing episodic processes  
420 (years to millennia): the role of pressure solution, *Oil and Gas Science and Technology—Revue d'IFP Energies*  
421 *nouvelles*, 66(3), 491-506.
- 422 Gratier, J. P., and Gueydan, F., 2007, Effect of Fracturing and Fluid–Rock Interaction on Seismic Cycles, *Tectonic*  
423 *Faults: Agents of Change on a Dynamic Earth*, 95, 319e356.
- 424 Gureyev, TE, Nesterets, Y, Ternovski, D, Wilkins, SW, Stevenson, AW, Sakellariou, A and Taylor, JA 2011,  
425 Toolbox for advanced x-ray image processing, in *Advances in Computational Methods for X-Ray Optics II* edited  
426 by M Sanchez del Rio and O Chubar, *Advances in Computational Methods for X-Ray Optics II*, San Diego, USA,  
427 21-25 August 2011: SPIE - The International Society of Optics and Photonics 8141.
- 428 [Iassonov, P., Gebrenegus, T., and Tuller, M., 2009, Segmentation of X-ray computed tomography images of porous](#)  
429 [materials: A crucial step for characterization and quantitative analysis of pore structures. \*Water resources research\*,](#)  
430 [45\(9\), W09415, doi:10.1029/2009WR008087.](#)
- 431 Janssen, C., Wirth, R., Reinicke, A., Rybacki, E., Naumann, R., Wenk, H. R., and Dresen, G., 2011, Nanoscale  
432 porosity in SAFOD core samples (San Andreas Fault), *Earth and Planetary Science Letters*, 301(1), 179-189.
- 433 [Hapca, S. M., Houston, A. N., Otten, W., and Baveye, P. C., 2013, New local thresholding method for soil images](#)  
434 [by minimizing grayscale intra-class variance, \*Vadose Zone Journal\*, 12\(3\), 12 \(3\): vzj2012.0172.](#)
- 435 Labaume, P., Maltman, A. J., Bolton, A., Tessier, D., Ogawa, Y., and Takizawa, S. 1997, Scaly fabrics in sheared  
436 clays from the décollement zone of the Barbados accretionary prism, in Shipley, T.H., Ogawa, Y., Blum, P., and  
437 Bahr, J.M. (Eds.), *Proceedings of the Ocean Drilling Program Scientific Results*, 59-78.
- 438 Kirilova, M., Toy, V. G., Timms, N., Halfpenny, A., Menzies, C., Craw, D., [Beysac, O., Sutherland, R., Townend,](#)  
439 [J., Boulton, C., Carpenter, B., Cooper, A., Grieve, J., Little, T., Morales, L., Morgan, C., Mori, H., Sauer, K.,](#)  
440 [Schleicher, A., Williams, J., and Craw, L., and Carpenter, B.-M.,](#) 2017, Textural changes of graphitic carbon by  
441 tectonic and hydrothermal processes in an active plate boundary fault zone, Alpine Fault, New Zealand, *Geological*  
442 *Society, London, Special Publications*, 453, SP453-13.
- 443 [Ma, X., Kittikunakorn, N., Sorman, B., Xi, H., Chen, A., Marsh, M., Mongeau, A., Piché, N., WilliamsIII, E. O.,](#)  
444 [and Skomski, D., 2020, Application of Deep Learning Convolutional Neural Networks for Internal Tablet Defect](#)  
445 [Detection: High Accuracy, Throughput, and Adaptability, \*Journal of Pharmaceutical Sciences\*, 109\(4\), 1447-1457.](#)
- 446 [Macente, A., Vanorio, T., Miller, K. J., Fousseis, F., and Butler, I. B., 2019, Dynamic Evolution of Permeability in](#)  
447 [Response to Chemo-Mechanical Compaction, \*Journal of Geophysical Research: Solid Earth\*, 124\(11\), 11204-11217.](#)
- 448 Marone, C., Raleigh, C. B., and Scholz, C. H., 1990, Frictional behavior and constitutive modeling of simulated  
449 fault gouge, *Journal of Geophysical Research: Solid Earth*, 95(B5), 7007-7025.
- 450 Niemeijer, A., Marone, C., and Elsworth, D., 2010, Fabric induced weakness of tectonic faults, *Geophysical*  
451 *Research Letters*, 37, L03304, doi:10.1029/2009GL041689.
- 452 Norris, R. J., and Cooper, A. F., 1995, Origin of small-scale segmentation and transpressional thrusting along the  
453 Alpine fault, New Zealand. *Geological Society of America Bulletin*, 107(2), 231-240.
- 454 Norris, R. J., and Cooper, A. F., 2001, Late Quaternary slip rates and slip partitioning on the Alpine Fault, New  
455 Zealand. *Journal of Structural Geology*, 23(2), 507-520.

- 456 Norris, R. J., and Toy, V. G., 2014, Continental transforms: A view from the Alpine Fault, *Journal of Structural*  
457 *Geology*, 64, 3-31.
- 458 Renard, F., Gratier, J. P., and Jamtveit, B., 2000, Kinetics of crack-sealing, intergranular pressure solution, and  
459 compaction around active faults, *Journal of Structural Geology*, 22(10), 1395-1407.
- 460 [Renard, F., McBeck, J., Cordonnier, B., Zheng, X., Kandula, N., Sanchez, J. R., Kobchenko, M., Noiriel, C., Zhu,](#)  
461 [W., Meakin, P., Fousseis, F., and Dag K. Dysthe., & Fousseis, F., 2019, Dynamic in situ three-dimensional imaging](#)  
462 [and digital volume correlation analysis to quantify strain localization and fracture coalescence in sandstone, \*Pure\*](#)  
463 [and \*Applied Geophysics\*, 176\(3\), 1083-1115.](#)
- 464 Rice, J. R., 1992, Fault stress states, pore pressure distributions, and the weakness of the San Andreas fault,  
465 *International Geophysics*, 51, 475-503.
- 466 Rutter, E. H., and Elliott, D., 1976, The kinetics of rock deformation by pressure solution, *Philosophical*  
467 *Transactions for the Royal Society of London, Series A, Mathematical and Physical Sciences*, 283, 203-219.
- 468 Rutter, E. H., Hackston, A. J., Yeatman, E., Brodie, K. H., Mecklenburgh, J., and May, S. E., 2013, Reduction of  
469 friction on geological faults by weak-phase smearing, *Journal of Structural Geology*, 51, 52-60.
- 470 Schleicher, A. M., Sutherland, R., Townend, J., Toy, V. G., and Van Der Pluijm, B. A., 2015, Clay mineral  
471 formation and fabric development in the DFDP-1B borehole, central Alpine Fault, New Zealand, *New Zealand*  
472 *Journal of Geology and Geophysics*, 58(1), 13-21.
- 473 Schuck, B., Schleicher, A. M., Janssen, C., Toy, V. G., and Dresen, G., 2020, Fault zone architecture of a large  
474 plate-bounding strike-slip fault: a case study from the Alpine Fault, New Zealand. *Solid Earth*, 11(1), 95-124.
- 475 Secor, D. T., 1965, Role of fluid pressure in jointing, *American Journal of Science*, 263(8), 633-646.
- 476 Sibson, R. H., 1990, Conditions for fault-valve behaviour, *Geological Society, London, Special Publications*, 54(1),  
477 15-28.
- 478 Sleep, N. H., and Blanpied, M. L., 1992, Creep, compaction and the weak rheology of major faults, *Nature*,  
479 359(6397), 687-692.
- 480 Surma, F., Géraud, Y., and Pezard, P., 2003, Porosity network of the Nojima fault zone in the Hirabayashi hole  
481 (Japan), *in EGS-AGU-EUG Joint Assembly*.
- 482 Sutherland, R., Eberhart-Phillips, D., Harris, R. A., Stern, T., Beavan, J., Ellis, S Henrys, S., Cox, S., Norris, R.J.,  
483 Berryman, K.R. and Townend, J., 2007, Do great earthquakes occur on the Alpine fault in central South Island, New  
484 Zealand?, *In: A continental plate boundary: tectonics at South Island, New Zealand, Geophysical Monograph*,  
485 *American Geophysical Union*, 235-251.
- 486 Sutherland, R., Toy, V. G., Townend, J., Cox, S. C., Eccles, J. D., Faulkner, D. R Prior, D.J., Norris, R.J., Mariani,  
487 E., Boulton, C. and Carpenter, B.M., 2012, Drilling reveals fluid control on architecture and rupture of the Alpine  
488 fault, *New Zealand, Geology*, 40(12), 1143-1146.
- 489 Sutherland, R., Townend, J., Toy, V., Upton, P., Coussens, J., Allen, M., and Boles, A., 2017, Extreme  
490 hydrothermal conditions at an active plate-bounding fault, *Nature*, 546, 137-140, doi: 10.1038/nature22355.

491 Toy, V. G., Boulton, C. J., Sutherland, R., Townend, J., Norris, R. J., Little, T. A., and Scott, H., 2015, Fault rock  
492 lithologies and architecture of the central Alpine fault, New Zealand, revealed by DFDP-1 drilling, *Lithosphere*,  
493 L395-1.

494 Toy, V. G., Sutherland, R., Townend, J., Allen, M., Becroft, L., Boles, A., Boulton, C., Carpenter, B., Cooper, A.,  
495 Cox, S., Daube, C., Faulkner, D., Halfpenny, A., Kato, N., Keys, S., Kirilova, M., Kometani, Y., Little, T., Mariani,  
496 E., Melosh, B., Menzies, C., Morales, L., Morgan, C., Mori, C., Niemeijer, A., ... and Zimmer, M., 2017, Bedrock  
497 Geology of DFDP-2B, Central Alpine Fault, New Zealand, *New Zealand Journal of Geology and Geophysics.*,  
498 60(4), 497-518.

499 Upton P. and Craw D., 2008, Modelling the role of graphite in development of a mineralised mid-crustal shear zone,  
500 Macraes mine, New Zealand, *Earth and Planetary Science Letters* 266: 245-255.

501 Walder, J., and Nur, A., 1984, Porosity reduction and crustal pore pressure development, *Journal of Geophysical*  
502 *Research: Solid Earth*, 89(B13), 11539-11548.

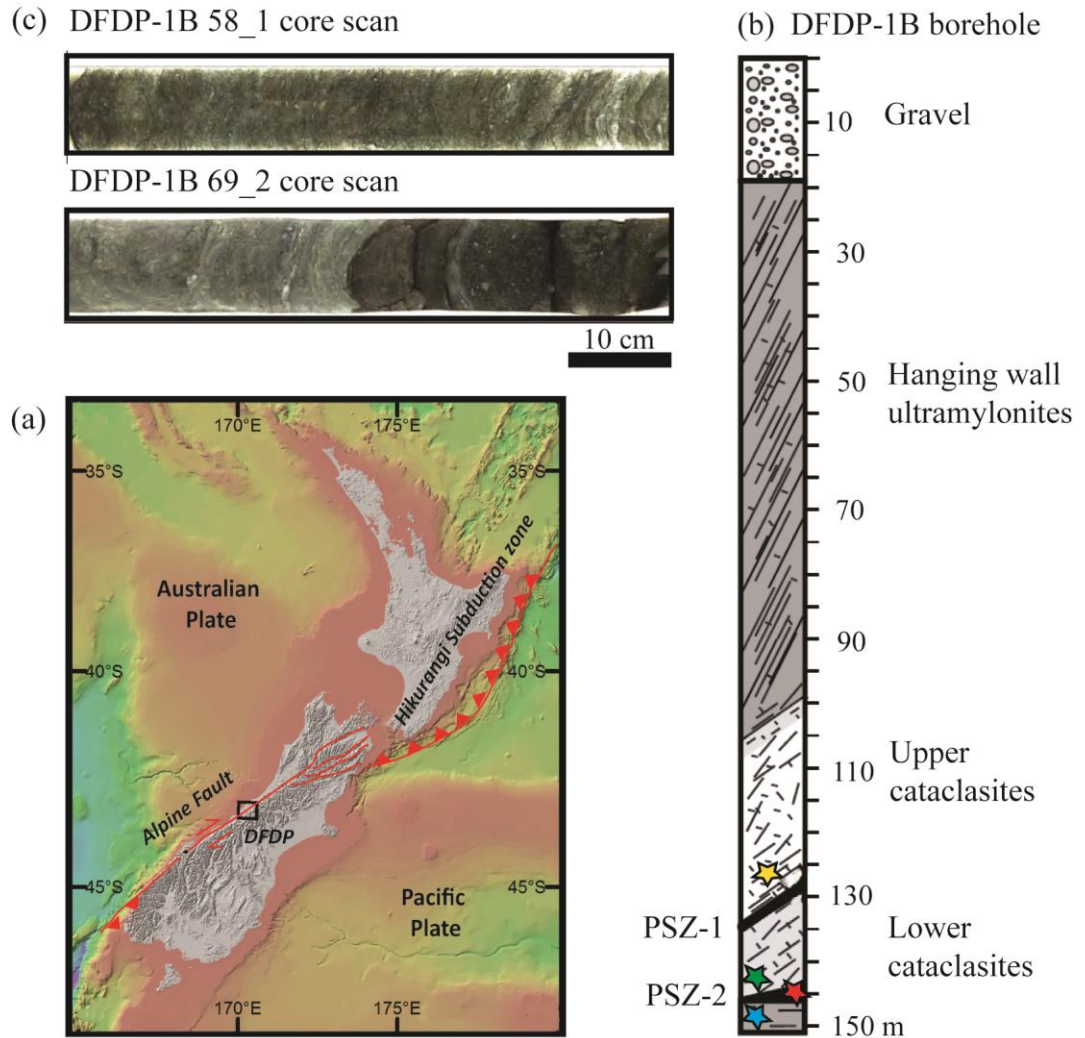
503 Walsh, J. B., 1965, The effect of cracks on the uniaxial elastic compression of rocks, *Journal of Geophysical*  
504 *Research*, 70(2), 399-411.

505 Wiersberg, T. and Erzinger, J., 2008, Origin and spatial distribution of gas at seismogenic depths of the San Andreas  
506 Fault from drill-mud gas analysis: *Applied Geochemistry*, v. 23, no. 6, p. 1675-1690.

507 Williams, J. N., Toy, V. G., Smith, S. A. and Boulton, C., 2017, Fracturing, fluid-rock interaction and mineralisation  
508 during the seismic cycle along the Alpine Fault, *Journal of Structural Geology*, 103, 151-166.

509 [Zhu, W., Allison, K. L., Dunham, E. M., Yang, Y., 2020, Fault valving and pore pressure evolution in simulations of](#)  
510 [earthquake sequences and aseismic slip, \*Nature Communications\*, 11, 4833, doi.org/10.1038/s41467-020-18598-z.](#)

511

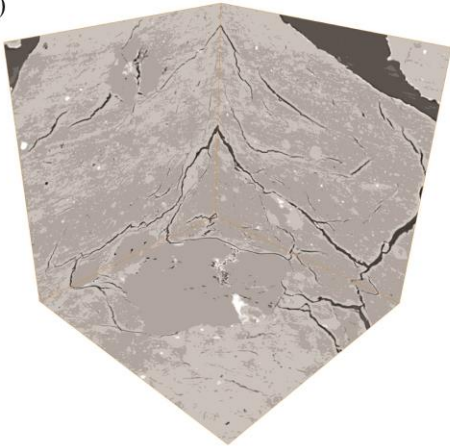


513

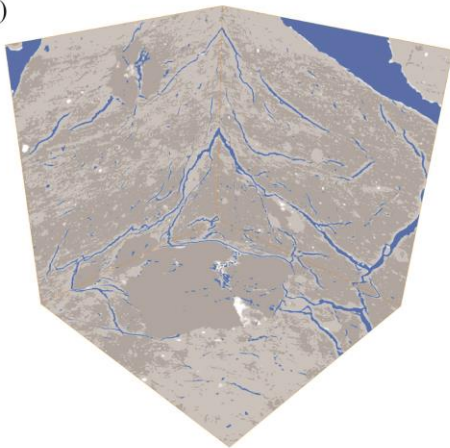
514 **Figure 1.** (a) Location map of DFDP drill sites (a bathymetric map compiled by NIWA). Drill site coordinates:  
 515 43°17'5"S, 170°24'22"E (b) Schematic diagram of the sampled lithologies in DFDP-1B borehole (modified after  
 516 Sutherland et al., 2012). (c) Scans of DFDP-1B drill core. Samples were collected from the locations indicated with  
 517 stars: yellow – DFDP-1B 58\_1.9; green – DFDP-1B 69\_2.48; red – DFDP-1B 69\_2.54; blue – DFDP-1B 69\_2.57.

DFDP - 1B 69-2.57

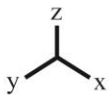
(a)



(b)



(c)



518

519

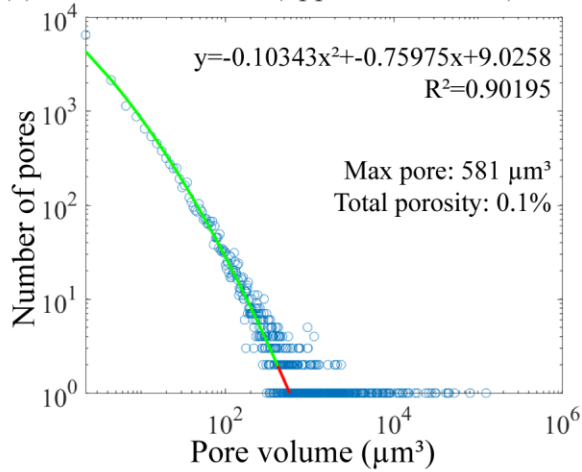
520

521

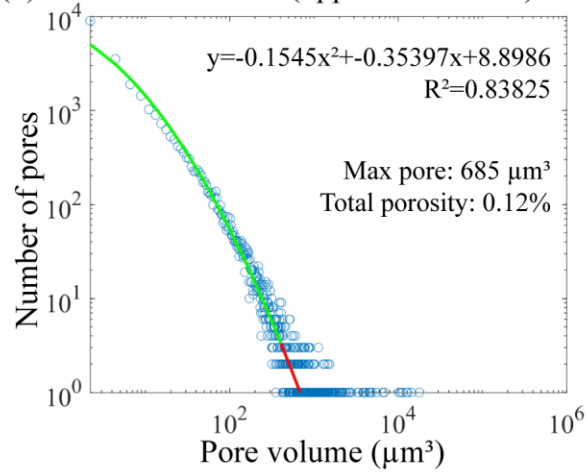
522

**Figure 2.** X-ray tomography data processing workflow. (a) Gray scale images in xy, xz and yz directions (b) Threshold of the darkest gray scale phase in each sample, corresponding to voids (pores and fractures); (c) 3D volume of the segmented pore spaces after removal of the fractures due to sample decompaction and coring damaging effects ~~were removed~~.

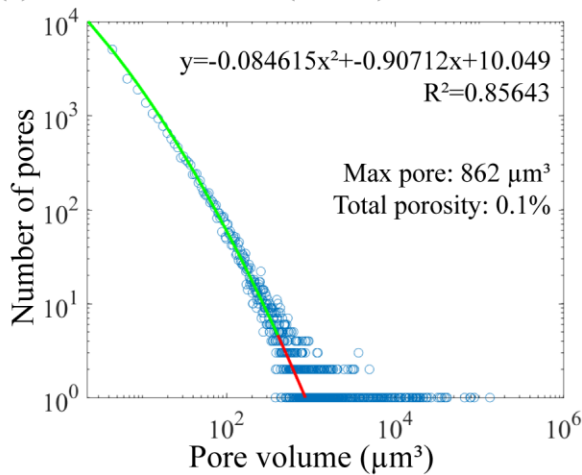
(a) DFDP-1B 58-1.9 (upper foliated ccl)



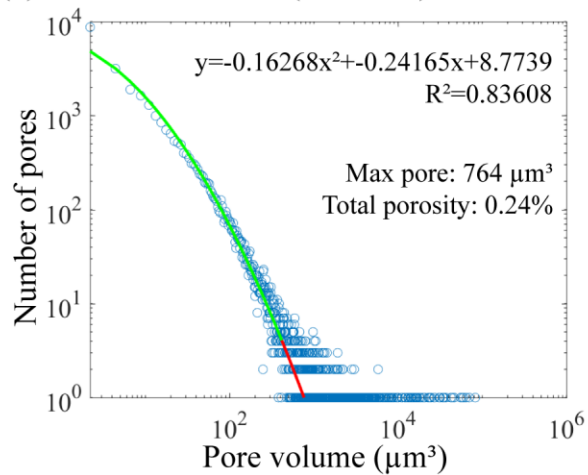
(b) DFDP-1B 69-2.48 (upper foliated ccl)



(c) DFDP-1B 69-2.54 (PSZ-2)



(d) DFDP-1B 69-2.57 (lower ccl)



523

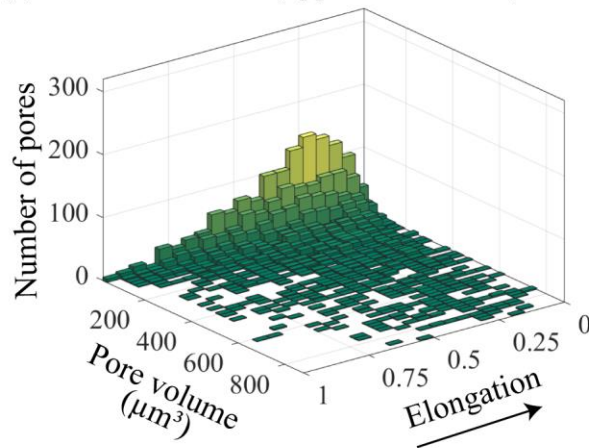
524

525

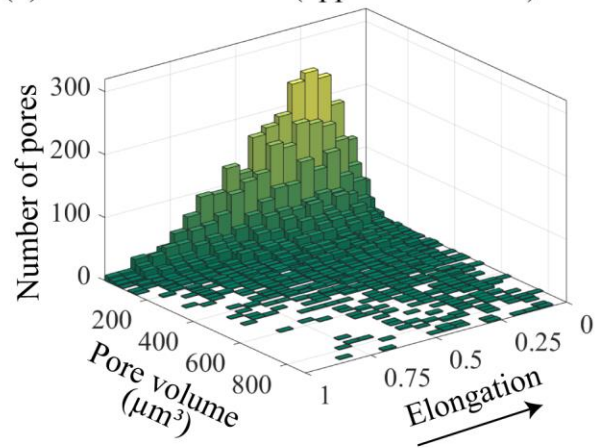
**Figure 3.** Plots of pore volume versus number of pores for each sample. Estimates of total porosity and size of the maximum expected pore are also shown, as well as the curve fitting function for each dataset.



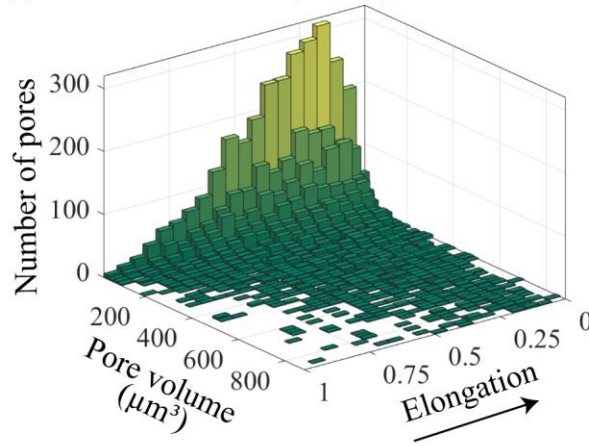
(a) DFDP-1B 58-1.9 (upper foliated ccl)



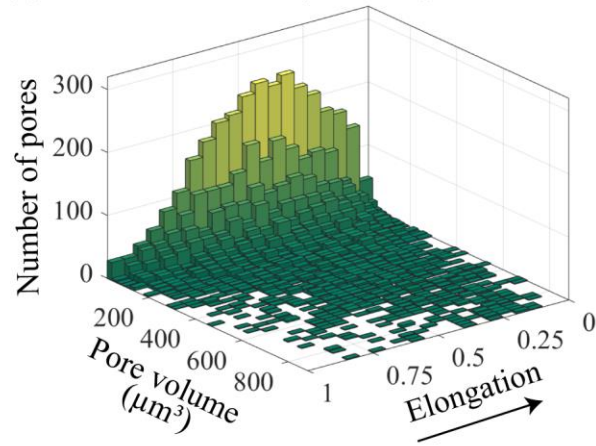
(b) DFDP-1B 69-2.48 (upper foliated ccl)



(c) DFDP-1B 69-2.54 (PSZ-2)



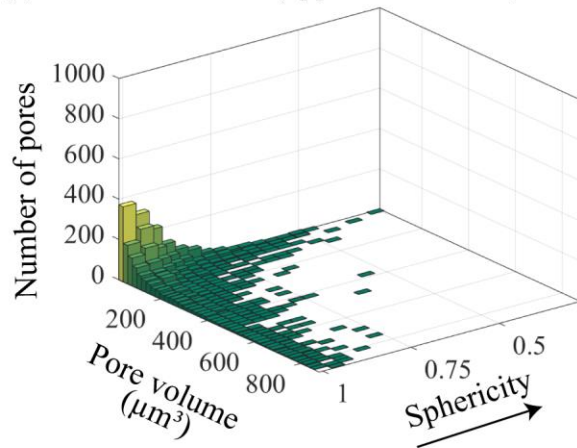
(d) DFDP-1B 69-2.57 (lower ccl)



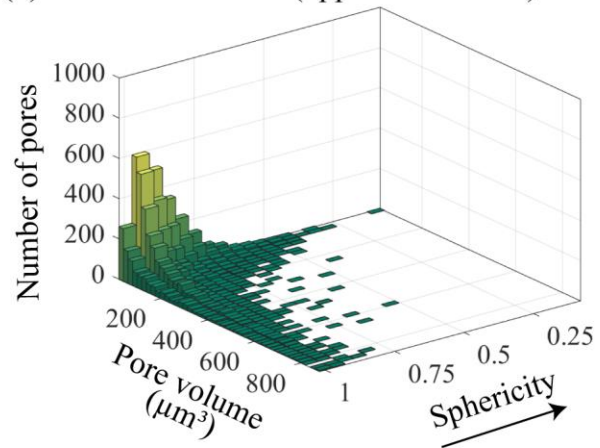
526

527 **Figure 4.** Bivariate histograms showing elongation versus pore volume ( $\mu\text{m}^3$ ) and number of pores for each sample.  
528 The arrow indicates the direction of increasing elongation. [Here, the elongation is defined as the ratio between the](#)  
529 [medium and the largest eigenvalues \(i.e. axis\) of each pore.](#)

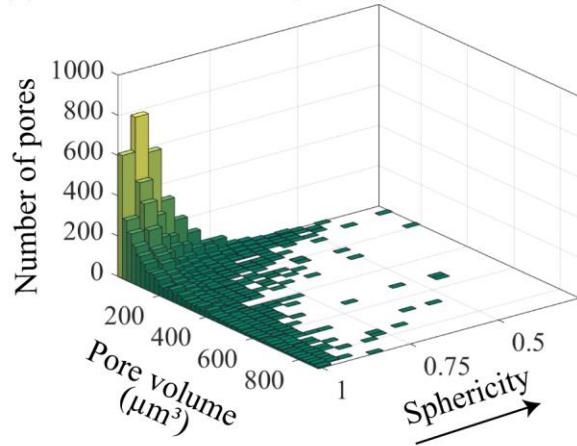
(a) DFDP-1B 58-1.9 (upper foliated ccl)



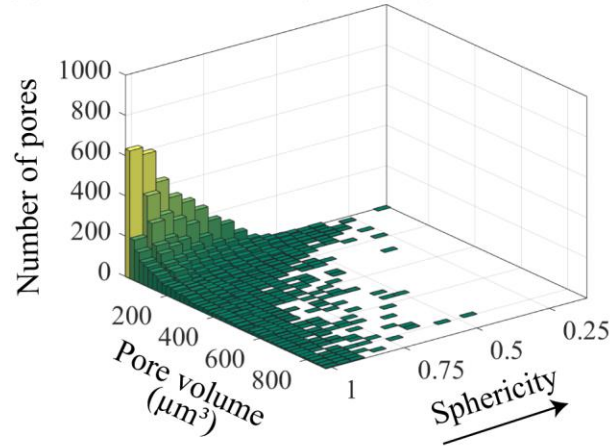
(b) DFDP-1B 69-2.48 (upper foliated ccl)



(c) DFDP-1B 69-2.54 (PSZ-2)



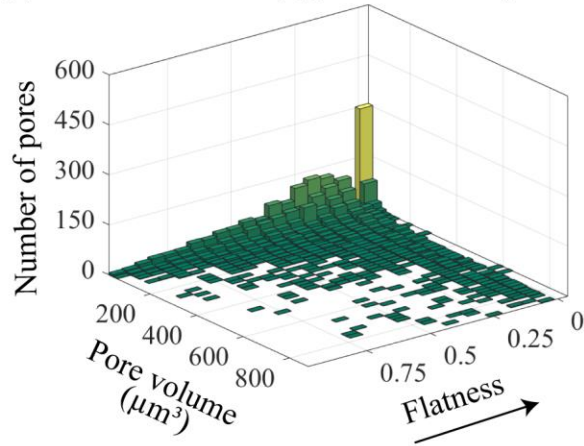
(d) DFDP-1B 69-2.57 (lower ccl)



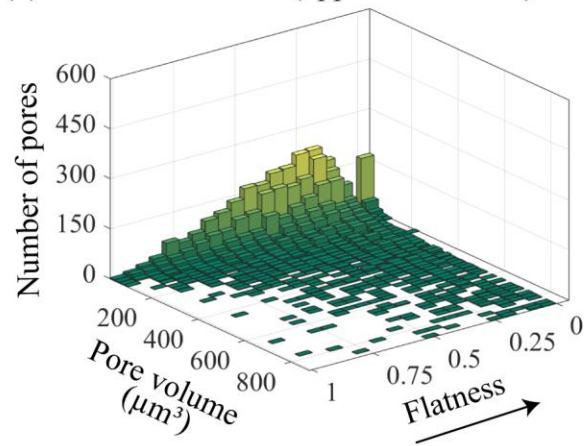
530

531 **Figure 5.** Bivariate histograms showing sphericity versus pore volume ( $\mu\text{m}^3$ ) and number of pores for each sample.  
532 The arrow indicates the direction of increasing sphericity. [Here, the sphericity is defined as the ratio between the](#)  
533 [smallest and the largest eigenvalues \(i.e. axis\) of each pore.](#)

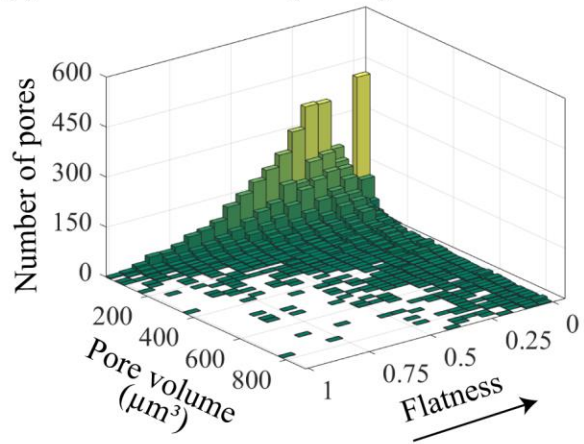
(a) DFDP-1B 58-1.9 (upper foliated ccl)



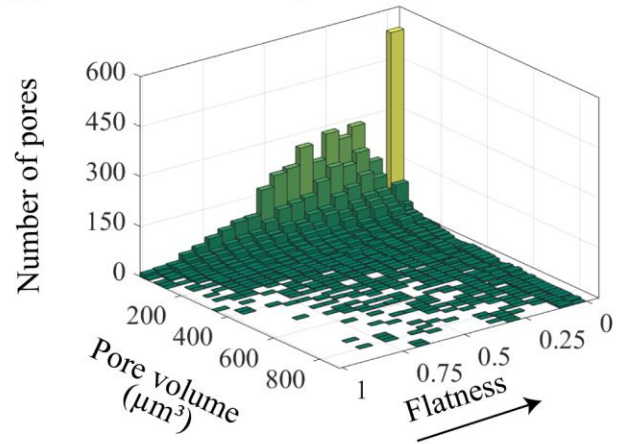
(b) DFDP-1B 69-2.48 (upper foliated ccl)



(c) DFDP-1B 69-2.54 (PSZ-2)



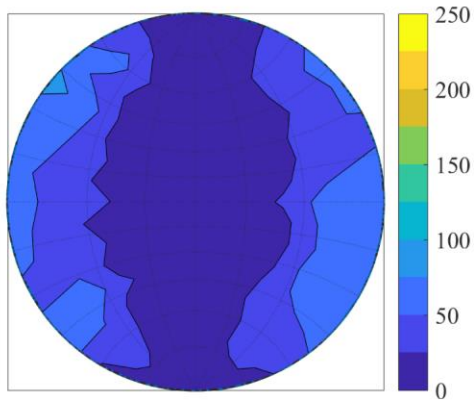
(d) DFDP-1B 69-2.57 (lower ccl)



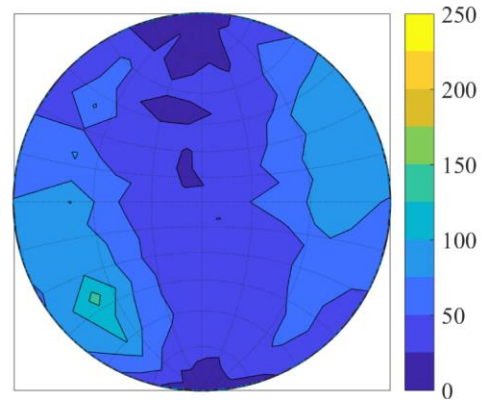
534

535 **Figure 6.** Bivariate histograms showing flatness versus pore volume ( $\mu\text{m}^3$ ) and number of pores for each sample.  
536 The arrow indicates the direction of increasing flatness. [Here, the flatness is defined as the ratio of the smallest and](#)  
537 [the medium eigenvalues \(i.e. axis\) of each pore.](#)

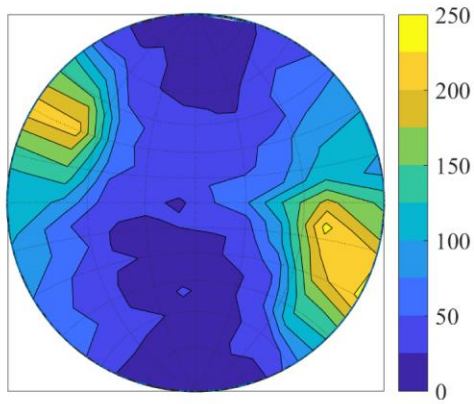
(a) DFDP-1B 58-1.9 (upper foliated ccl)



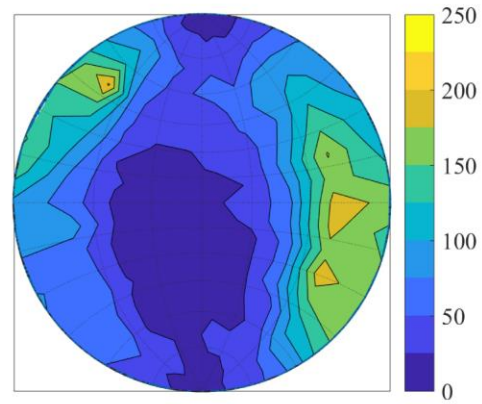
(b) DFDP-1B 69-2.48 (upper foliated ccl)



(c) DFDP-1B 69-2.54 (PSZ-2)



(d) DFDP-1B 69-2.57 (lower ccl)

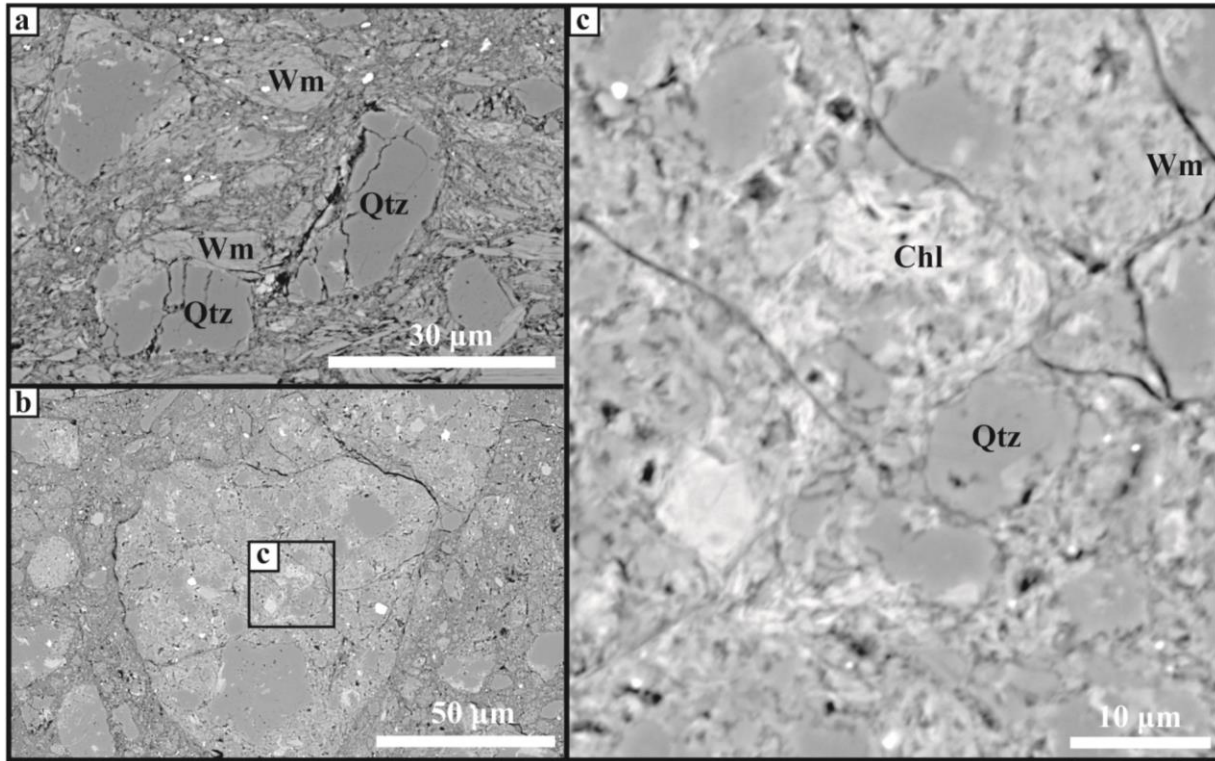


538

539

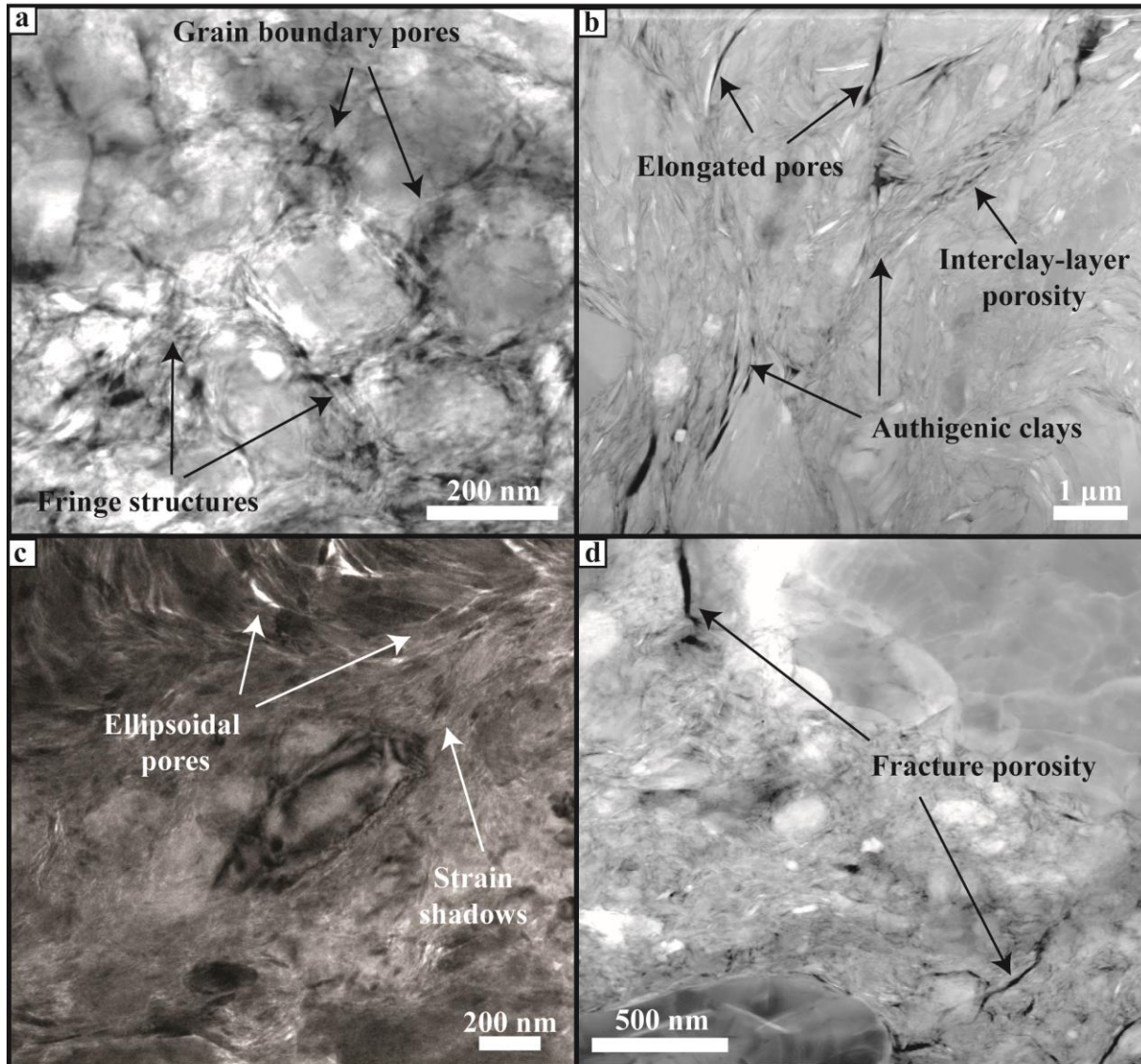
540

**Figure 7.** Distribution of pore unit orientations plotted on a lower hemisphere equal area stereographic projection with a probability density contour.



541

542 **Figure 8.** Scanning electron images collected from sample DFD 1B 69-2.48 showing the existing mineral  
 543 associations. (a) Sub-rounded and intensely fractured quartz and white mica clasts in association with white mica,  
 544 floating within fine matrix material. (b) Reworked cataclasite clasts in phyllosilicate-rich layer matrix. (c) Fine  
 545 chlorite and white mica fillings aggregates in-between quartz clasts. (Qtz = quartz, Wm = white mica, Chl = chlorite).



546

547 **Figure 9**. Transmission electron microscopy images collected ~~from~~ ~~from~~ the gouge sample DFDP-1B  
 548 69\_2.54 (PSZ-2). (a) and (c) are bright-field (BF) images, where porosity appears as bright contrast areas. (b) and  
 549 (d) are high-angle annular dark field (HAADF) images, where pores appear as dark contrast areas. (a) TEM bright-  
 550 field image of homogeneous fault gouge area. Quartz/feldspar grains, wrapped by fine authigenic clays, displaying  
 551 fringe ~~structures~~ ~~morphologies~~. Pores with sub-angular shape distributed along grain boundaries. (b) HAADF image  
 552 of phyllosilicate-rich gouge area. Co-existence of fine authigenic clays with coarser clay mineral grains. Elongated  
 553 pores and interlayer porosity. (c) TEM bright-field image of ellipsoidal pores in phyllosilicate-rich areas. Examples  
 554 of strain shadows along quartz/feldspar grains. (d) HAADF image of fracture porosity along grain boundaries of  
 555 quartz/feldspar grains.